Highlights

Superheated flash-boiling atomisation effects on spray carbon capture performance using non-aqueous amines

Louis F. Dacanay[*a], Kevin Wan[b], Julien Manin[b], Guillaume De Sercey[a], Peter J. Cragg[c], Alain Ledoux[d], Lionel Estel[d], Cyril Crua[e]

- More intense solvent flash boiling improves CO_2 absorption rates and capacities
- Increased environment temperature greatly enhances CO_2 capture performance
- Transitional flash boiling increased molar absorption rate by 4.5x
- Flash boiling carbon capture could support hard-to-abate sectors

Superheated flash-boiling atomisation effects on spray carbon capture performance using non-aqueous amines

Louis F. Dacanay[*a], Kevin Wan[b], Julien Manin[b], Guillaume De Sercey[a], Peter J. Cragg[c], Alain Ledoux[d], Lionel Estel[d], Cyril Crua[e]

[a]*Advanced Engineering Centre, University of Brighton, Brighton, BN2 4GJ, United Kingdom*
[b]*Combustion Research Facility, Sandia National Laboratories, 7011 East Ave, 94550 Livermore, USA*
[c]*School of Applied Sciences, University of Brighton, Huxley building, Brighton, BN2 4GJ, East Sussex, UK*
[d]*Laboratory for Chemical Process Safety, Université de Rouen Normandie, INSA Rouen, Avenue de l'Université – Saint-Étienne-du-Rouvray cedex, 76801 France*
[e]*Energy and Materials Engineering Research Centre, University of Sussex, Brighton, BN1 9RS, UK*

Abstract

There is an urgent need to develop energy and space efficient carbon capture technologies for hard to decarbonise sectors. While spray-based carbon capture systems can offer high CO_2 absorption rates compared to packed columns, their optimisation requires fine control on spray homogeneity and droplet properties such as size and relative velocity. More specifically, denser mono-disperse sprays with micron scale droplets have been found to increase the rate of CO_2 absorption due to increased surface area for mass transfer. One approach that has not previously been investigated is to control the solvent spray properties through flash boiling atomisation to consistently produce fine and homogenous droplets. To address this gap, we present optical measurements comparing the performance of solvents atomised with varying degrees of flash boiling. Diffuse-back illumination extinction imaging was used for temporal characterisation of spray morphology. We tested a 20:80 (% w/w) blend of triethanolamine and methanol, and neat isopropylamine under six temperature conditions to vary the amount of superheat. Absorption capacities, molar absorption rates, and CO_2 percentage removal are reported for each test condition, showing significant improvements at the higher temperature conditions where flash boiling was more intense. While flash boiling carbon capture carries a higher energy demand than conventional technologies, our results offer an innovative and promising avenue for high-efficiency CO_2 absorption in hard-to-abate sectors such as marine transportation, especially when coupled with a waste heat recovery strategy.

Keywords: Non-aqueous amines, CO_2 molar absorption rate, absorption capacity, flash boiling

atomisation, superheat, IR gas detection

1. Introduction

Recent greenhouse gas projections have indicated that without a change in climate policy or technological reforms, achieving climate goals of net zero CO_2 by 2050 and limiting global warming to 1.5-2 °C this century will be a challenging task (Ritchie et al., 2020). Major governments have employed the use of CCS (carbon capture and storage) technologies within their nationwide strategies to mitigate CO_2 emissions (United Nations Framework Convention on Climate Change, 2015; UK Department for Energy Security et al., 2020). Post combustion gas purification via amine solvent absorption, being the most mature method for removing anthropogenic emissions, has been listed as a key technology in achieving global climate goals (Environment Agency, 2021). The conventional gas absorption process utilises two closed structures: An absorber column where the liquid amine is introduced top-side against the counterflowing flue gas at temperatures of 40-50 °C, and a stripper column where the rich amine is heated to release the captured CO_2 (at temperatures of 130-140 °C), after which the clean solvent is cycled back for reuse (Wu et al., 2014; Biliyok et al., 2012). CO_2 partial pressures in the absorber are low (0.1 to 1 bar), as post combustion flue gases consist of mainly nitrogen with little CO_2 (up to 15 vol%) (Gupta et al., 2003; Manalapally and Hasse, 2011). These columns are typically used for stationary heavy emitting sources such as cement/steel production and fossil-fuel powered energy plants (Adeosun and Abu-Zahra, 2013). Aqueous amine mixtures such as water and monoethanolamine (MEA), which is a primary amine and the current industry standard due to its low cost and high chemical reactivity, are typically utilised for scrubbing flue gases with lean amounts of CO_2 (Rochelle, 2009; Puxty et al., 2009; El Hadri et al., 2017). However, due to the high energy consumption related to the regeneration of monoethanolamine, alternatives are required to make amine absorption technology more economically viable (Li et al., 2016). Tertiary amines are theoretically more efficient in terms of capacity than primary or secondary amines,

*Corresponding author: Louis F. Dacanay. Tel.:+44 7846705439
Email addresses: e.dacanay2@uni.brighton.ac.uk (Louis F. Dacanay[*a]), kwan@sandia.gov (Kevin Wan[b]), jmanin@sandia.gov (Julien Manin[b]), g.desercey@brighton.ac.uk (Guillaume De Sercey[a]), p.j.cragg@brighton.ac.uk (Peter J. Cragg[c]), alain.ledoux@insa-rouen.fr (Alain Ledoux[d]), lionel.estel@insa-rouen.fr (Lionel Estel[d]), c.crua@sussex.ac.uk (Cyril Crua[e])

only requiring 1 mole of amine in solution to absorb 1 mole of CO_2 and are therefore being investigated as potential alternatives (Puxty et al., 2009; Xiao et al., 2016; Shen et al., 2018). Furthermore, the use of non-aqueous amine mixtures have been found to provide benefits such as increased cyclic capture capacities, minimised amine degradation, and significant reduction in energy consumption during solvent regeneration (Lai et al., 2019; Guo et al., 2019; Hwang et al., 2019).

CO_2 absorption is achieved using absorption contactors (e.g. packed columns, trays, and sprays) within the absorber column that aim to increase the surface area contact between the liquid chemical absorbent and flue gas (Kohl and Nielsen, 1997). Sprays have been found to perform better than packed columns and trays because of increased volumetric mass transfer from the larger gas-liquid interfacial area provided by droplets (Kuntz and Adisorn, 2009). Furthermore, sprays offer minimal pressure drop and have low maintenance costs due to their simple requirements (Seyboth et al., 2014). Liquid droplet size has been reported to correlate directly with CO_2 absorption performance (Tamhankar et al., 2014). Smaller droplets (Sauter mean diameter $< 50\,\mu m$ at lab scale) increased the absorption rate and overall CO_2 removal due to the increased overall liquid surface area and reduced diffusion time for the gas molecules across each droplet (Cho et al., 2018; Kavoshi et al., 2015; Ouboukhlik et al., 2015a). A polydisperse spray lowers the overall average absorption capacity due to its large size distribution and thus irregular CO_2 diffusion time per droplet (Cho et al., 2018). Therefore, homogeneous mono dispersed sprays are favoured as they offer more control over absorption rate, larger absorption capacities, and decrease the pressure drop more effectively given low gas flow rates (Cho et al., 2018; Michalski, 2000). A universally optimal droplet size has yet to be defined for spray capture as it is dependent on a variety of operational conditions and absorber properties (e.g., gas flow rate, injection pressure, liquid flow rate). While smaller droplet diameters extend absorption capabilities, the droplets are more likely to fly back and collide with the column wall from the high velocity counter-flowing gas, resulting in the formation of liquid films which decrease capture performance (Seyboth et al., 2014). Faster droplet velocities, caused by higher injection pressures, may reduce the CO_2 capture efficiency due to shorter residence time, although this can be balanced with faster reacting solvents or adjusting spray direction relative to the gas (e.g. upward scheme) (Xu et al., 2021). Regardless, there is a consensus that indicates operating with a smaller droplet regime yields a higher capture performance (Cho et al., 2018; Kavoshi et al., 2015; Ouboukhlik et al., 2015a;

Javed et al., 2010; Kuntz and Adisorn, 2009; Zimmermann et al., 2017). Adjustment of the injector design remains the primary method of modifying liquid solvent atomisation characteristics for CO_2 spray capture. Some examples include the use of a full cone nozzle, ultrasonic nozzle, spiral tip and swirl chamber nozzle, and pressure swirl atomiser (Cho et al., 2018; Ouboukhlik et al., 2015b; Stolaroff et al., 2010; Javed et al., 2010). None have explored adjusting the capture chamber conditions to achieve more intense spray atomisation and mixing using the flash boiling mechanism, which is commonly observed in modern direct injection engines (She et al., 2010; Senda et al., 2008).

Flash boiling atomisation occurs when a liquid is brought into a metastable superheated state, specifically when the environment pressure the liquid is injected into is lower than the saturation pressure of the liquid itself (Reitz, 1990). The temperature of the liquid, in its pre-heated state, prior to injection and the ratio of its saturation pressure (P_{sat}), relative to environment pressure (P_{env}), dictates the degree of superheat (R_p). With different levels of R_p, the intensity of flash boiling can be controlled resulting in distinct spray regimes, namely non-flash boiling/subcooled ($R_p < 1$), transitional flash-boiling ($1 < R_p < 3.33$), and flare flash-boiling ($R_p > 3.33$) (Zeng et al., 2012; Kapusta, 2022). This form of breakup has been reported to produce consistently fine droplets (SMD $< 50\,\mu m$) and high droplet number densities (up to 18,000 droplets$/mm^3$) at a liquid temperature range of 20-109 °C and injection pressure of 5 MPa (Shen et al., 2016). Furthermore, with a greater degree of R_p, a narrowing of the spray plume angle is observed and may also reduce the penetration of the spray/jet (Zeng et al., 2012). Given these properties, sprays adopting the flash boiling atomisation mechanism will most likely be suited for systems involving slow gas flow fields to prevent the finer droplets from colliding with the chamber/column wall and producing liquid films which has been linked to significantly limit the CO_2 captured (Seyboth et al., 2014). Hence, applications involving lower gas flow rates such as energy plant/factory absorption columns and reactor systems would be ideal. As flash boiled sprays are reliant on raising the temperature of the solvent to induce superheat and trigger the atomisation process, they may also be used with systems that release high temperature exhaust gases from large scale combustion engines (e.g. maritime transport machinery) when coupled with waste heat recovery units. This can create an economical heat recovery capture cycle and introduce further energy saving benefits but will likely require a method of slowing down the exhaust gas

flow rate to fully optimise the absorption process. Although spray properties generated via flash boiling atomisation are particularly attractive for CO_2 absorption applications, it appears that no previous research has been published on this particular approach within the context of carbon capture. To address this gap, we provide quantitative results on overall CO_2 absorption when taking advantage of the flash boiling mechanism for liquid solvent atomisation. The objective was to examine the effects of varying superheating degree of the solvent on capture performance using a triethanolamine-methanol blend and neat isopropylamine as examples of a tertiary and primary amines, respectively. Methanol was chosen to mix with triethanolamine primarily to reduce the specific heat of the solvent and decrease the energy required for thermal regeneration compared to aqueous blends. Further benefits of using methanol over water are its tendency to enhance solubility, diffusive properties, and CO_2 mass transfer (Sema et al., 2013; Usubharatana and Tontiwachwuthikul , 2009). Absorption capacities and molar absorption rates of the solvent blend over the range of injector nozzle and chamber temperature conditions and subsequent CO_2 concentration drops are reported.

2. Materials and methods

2.1. Apparatus and approach

The experimental design consisted of Sandia's constant volume spray vessel with an internal volume of 1000 cm^3 (more details available at Pickett et al. (2010)), a high-speed CMOS camera, a high-speed MWIR (mid-wave infrared) camera, and an LED light source. A single-hole hollow cone no-swirl injector (Bosch HDEV-1-1HF, 06F906036A), with an orifice diameter of 0.66 mm (Gaur, Saha, and Ghai , 2024), was mounted at the northern port of the chamber for atomising the solvent blend into the spray vessel. A Teledyne 30D syringe pump was used to pressurise the solvent to 4 MPa and record the injected volume. Diffuse backlit imaging (DBI) was implemented using the high-speed CMOS camera (Phantom v2512) positioned at the eastern port of the chamber perpendicular to the injection direction, and a 520 nm wavelength LED emitter operating at a pulse duration of 200 ns with diffuser directly opposite at the western port. The Phantom V2512 was fitted with 50 mm f/1.8 and 500D close up lenses, with a 520 nm filter to match the LED, operated at 20 kHz with a frame size of 384×512 $pixel^2$, and had a spatial resolution of 3000 µm/pixel. During the injection period, DBI images of the spray morphology were captured to verify the occurrence of flash boiling. The MWIR camera (FLIR X6900sc) was operating at 1 kHz with a frame size of 576×512 $pixels^2$ and placed at the southern port facing directly towards the injector for MWIR imaging of the injector region. Fig. 1 displays a sectioned view of the spray vessel chamber and optical setup.

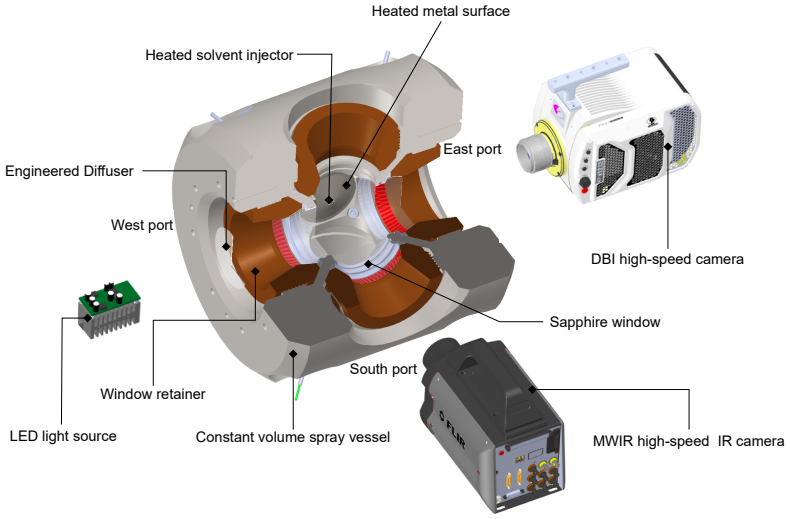

Figure 1: Schematic of experimental design displaying position of 532 nm LED, MWIR camera, and high-speed camera relative to the constant volume spray vessel and injector.

The MWIR camera was fitted with a bandpass filter (4.26 µm, 0.12 µm FWHM, Edmund Optics #84-073) to minimise the effect of non-CO_2 absorption (water, solvent) on the IR extinction recordings. A spectral chart displaying the transmission of IR radiation through the multiple species/components within the experimental setup is shown in Fig. 2.

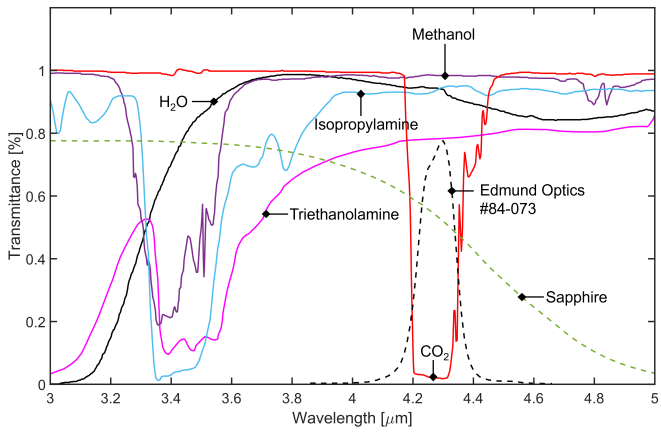

Figure 2: Spectral chart displaying transmissivity of IR radiation through the species/components present within the experimental setup

The spray vessel used sapphire windows at each of the open ports (east, west, and south) for optical access to the vessel's interior. The injector port and spray vessel were heated using independent PID temperature control systems. The injector itself was mounted in a stainless-steel port that was heated using six cartridge heaters which surrounded the injector tip. The interior of the spray vessel from the point of view of the MWIR camera is shown in Fig 3. Inlet and exhaust valves used for CO_2 filling and purging were located at the top and bottom corners of the spray vessel. A fan was operated in the vessel at approximately 1000 rpm to ensure that the CO_2 absorption was homogeneous within the camera's field of view, and to avoid thermal stratification. During the solvent injection, the gas inlet and exhaust valves of the spray vessel were shut, therefore there was no continuous flow of CO_2 into the chamber during the absorption process. This differs from typical gas scrubbing columns where flue gas is continuously fed into the tower counter current to the injected solvent. This forms a limitation for this work as it does not account for the impact of gas flow rate on capture performance.

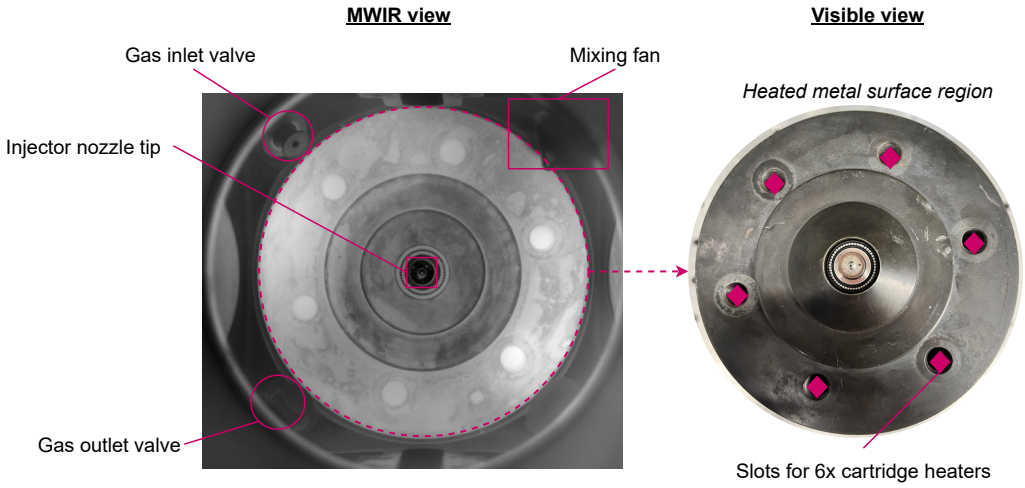

Figure 3: Infrared view of the chamber from the MWIR camera with annotations for the key components within view (*left*). A visible view snippet of the injector nozzle tip is also included, showing the single orifice near the centre of the tip (*right*).

The rationale for an IR optical approach was to gather quantitative CO_2 gas concentrations at specific regions of the chamber during and after the injection process, which could then be used to determine the absorption rate. It was also used to confirm the spray structure and degree of flash boiling. Finally, optical imaging methods offer the capability of mapping out spatial and

temporal evolution of gas concentrations within the chamber pre, post, and during solvent injection. The IR images captured were within the MWIR spectral band, specifically near the 4.26 µm wavelength with 0.12 µm FWHM (full-width half-maximum). IR videos were captured when the vessel was filled with N_2 as a reference point (at 0 % CO_2 gas), during the CO_2 filling process, injection period, and the CO_2 purging process. Each test point (Table 2) consisted in a total of 8 injection videos, with each video having 4 solvent injections (hence a total of 32 injections per test point). To quantify CO_2 concentrations from the IR images, correlations were made between image intensities and CO_2 gas densities. Fig. 4 shows a simplified diagram for the IR radiation transfer occurring from the heated injector nozzle and metal surface towards the thermal sensor within the IR camera. Some components within the experiment emitted and/or absorbed IR radiation within the recorded spectral band, including the CO_2 gas which simultaneously emitted and absorbed at the observed wavelength. Consequently, the absorption and emission of each individual component within the experiment had to be considered in order to compute the CO_2 concentration from the recorded IR intensities.

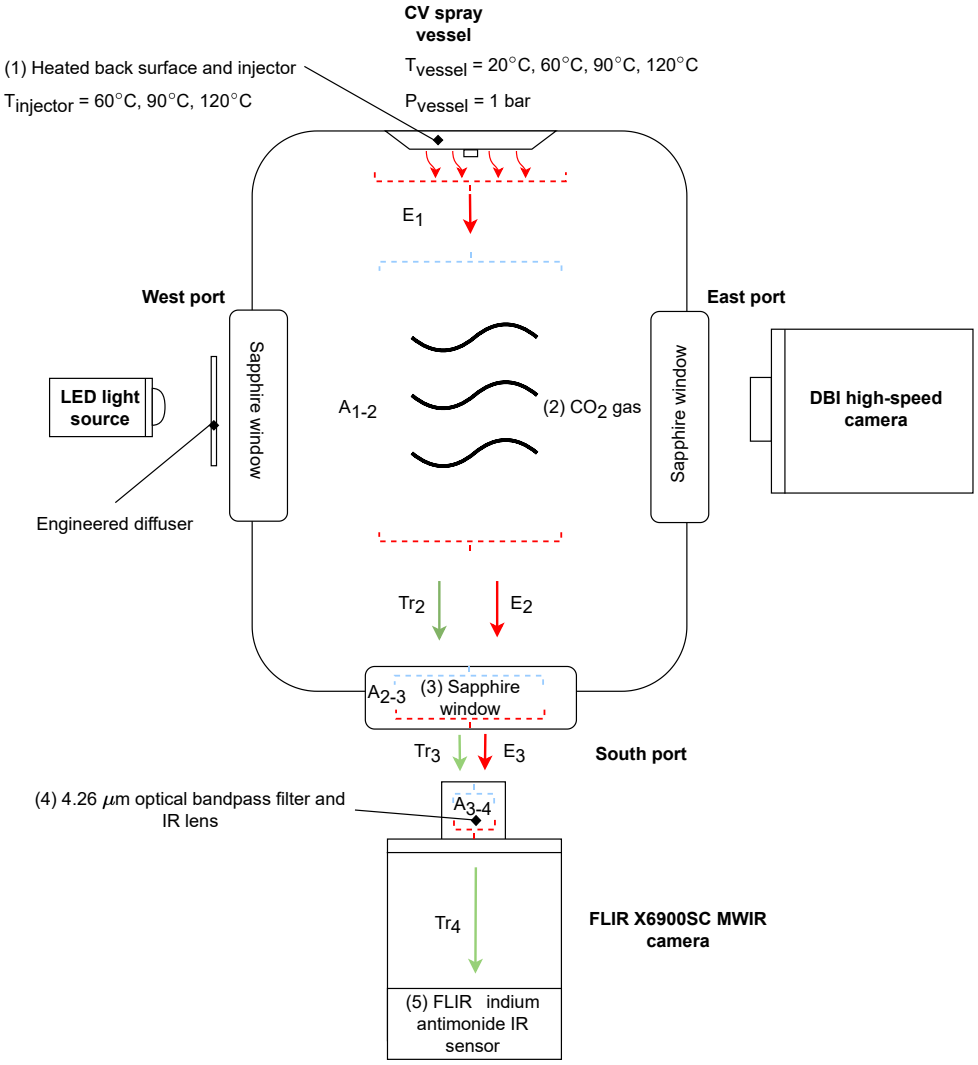

Figure 4: Heat transfer diagram starting from the heated metal surface/injector towards the MWIR camera. Each absorbing/emitting component in the rig is numbered (1-5). Labels "A" indicate points where IR absorption takes place (e.g. $A_{1\text{-}2}$ indicates absorption of incident radiation coming from the injector by the CO_2 gas). Labels "E" indicate IR emission sources (e.g. E_2 indicates emission from the CO_2 gas). Labels "Tr" indicate transmitted IR radiation (e.g. T_{r2} represents IR radiation transmitted through the CO_2 gas

2.2. *Radiative heat transfer equation (RTE)*

The radiative heat transfer equation (abbreviated to RTE) describing the change of intensity (at a specific spectral range) with optical distance through a medium (in this case CO_2) that simultaneously absorbs and emits (neglecting scattering effects) is shown in Equation 1 (Modest and Mazumder, 2021):

$$\frac{dI_\eta}{ds} = \kappa_\eta(I_{b\eta} - I_{\eta,0}) \tag{1}$$

where I_η is the transmitted (i.e. spatially attenuated) intensity [pixel counts], κ_η [m^{-1}] is the linear absorption coefficient of CO_2 , $I_{b\eta}$ [pixel counts] is the blackbody radiation of the CO_2, $I_{\eta,0}$ [pixel counts] is the incident intensity entering the CO_2 volume, and s [m] is the path length through the CO_2. The product of κ_η and $I_{b\eta}$ refers to emission of the CO_2 and is proportional to the gas volume. The product of κ_η and -$I_{\eta,0}$ relates to the CO_2 absorption and is negative due to light intensity decreasing as it propagates through the gas. The linear absorption coefficient of CO_2 is calculated experimentally using the Lambert's attenuation law in Equation 2 (Oshina and Spigulis, 2021):

$$\kappa_\eta = \frac{\ln(\frac{I_\eta}{I_{\eta,0}})}{s} \tag{2}$$

2.2.1. *Solution to the RTE and final modelling equation*

For an isothermal gas layer with thickness s, the transmitted intensity, neglecting light scattering, can be obtained by integrating Equation 1 over the path distance (Modest and Mazumder, 2021):

$$I_\eta(s) = I_{\eta,0}\exp(-\tau_\eta) + I_{b\eta}(1 - \exp(-\tau_\eta)) \tag{3}$$

Note that $\exp(-\tau_\eta)$ equates to transmission, therefore 1 minus this value will give the absorption. When the absorption is multiplied by the blackbody intensity of the CO_2 and given a positive sign, it results in the emission term. The entire term $(1 - \exp(-\tau_\eta))$ also represents the CO_2 emissivity. As there is an absorption constant A relating the absorption of external components such as optics (Sapphire, IR lens, and filter) as seen in Fig 4, Equation 3 is re-written as:

$$I_\eta(s) = AI_{\eta,0}\exp(-\kappa_{\rho\eta}s\rho_{CO_2}) + AI_{b\eta}\exp(-\kappa_{\rho\eta}s\rho_{CO_2}) \tag{4}$$

From Equation 4, constants A and $I_{b\eta}$ are experimentally unknown. Therefore, a simultaneous equation approach was taken to resolve this issue. Assuming a scenario where concentration is known, e.g. 100 % CO_2 environment, Equation 4 can be rearranged and solved for A as a function of $I_{b\eta}$:

$$A = \frac{I_{\eta,CO2,100}}{I_{\eta,0}\exp(-\kappa_{\rho\eta} s \rho_{CO_2,100}) + I_{b\eta}\exp(-\kappa_{\rho\eta} s \rho_{CO_2,100})} \tag{5}$$

where $I_{\eta,CO2,100}$ [pixel counts] is the intensity at 100 % CO_2 concentration, and $\rho_{CO_2,100}$ [kg m^{-3}] is the theoretical density of CO_2 at the experimental temperature and pressure conditions. Because A is an experimental constant, Equation 5 is substituted back into Equation 4 giving:

$$I_\eta = I_{\eta,CO2,100}\frac{I_{\eta,0}\exp(-\kappa_{\rho\eta} s \rho_{\mathrm{CO}_2}) + I_{b\eta}\exp(-\kappa_{\rho\eta} s \rho_{\mathrm{CO}_2})}{I_{\eta,0}\exp(-\kappa_{\rho\eta} s \rho_{CO_{2,100}}) + I_{b\eta}\exp(-\kappa_{\rho\eta} s \rho_{CO_{2,100}})} \tag{6}$$

where the only remaining unknown is the blackbody radiation of the CO_2 in the spray vessel, $I_{b\eta}$. $I_{b\eta}$ was computed iteratively until the output transmitted intensity I_η matched the experimental average intensity for a known CO_2 concentration, i.e. 100 % CO_2, prior to the first solvent injection. Equation 6 was used to build a model that was fitted to the experimental average intensities recorded from the high-speed IR videos. CO_2 densities at different time points, both pre- and post-solvent injection, could then be computed using the fitted model.

2.3. Image processing method

Fig. 5 summarises the image processing methodology adopted to extract average pixel intensities from the IR images in preparation for fitting to the mathematical concentration model. To correct any extra signal caused by the camera's own radiation, the process began with extracting dark image average counts during shutter closing and subtracting from the raw frames of each IR video (Fig 5A). A small number of saturated 'hot' pixels were corrected by replacing them with the average of neighbouring pixels (Fig. 5B). Background radiation and hot pixel corrected frames were then masked. The region of interest (ROI) chosen for the mask was located at the upper left high emissivity region of the chamber beneath a cartridge heater (Fig. 5C and 5D). Being more elevated and nearer the fan, for a more homogenous gas distribution, it was less sensitive to gas stratification. Additionally, no window fouling was observed in this area, ensuring optical clarity. As the injector orifice was angled downwards, solvent deposits from injections were observed on the lower half of the sapphire window, but did not affect the ROI. Averages were taken at the

start of the videos because, when the solvent was injected, the chamber cooled down and the pixel intensity decreased which could introduce errors into calculations of CO_2 concentrations. The gas heated up and thermally stabilised to the temperature of the vessel between each injection video, so the beginning of each injection video represented a period where the CO_2 was at local thermodynamic equilibrium. Equation 6 was then used to create a model for I_η and fitting with the mean pixel intensities from the image processing. This fitting process started by finding $I_{b\eta}$ through the method described in section 2.2.1, which leaves ρ_{CO_2} as the only unknown in Equation 6. The model was fitted over all experimental mean pixel intensities calculated from the image processing of 8 injection videos using least square-regression.

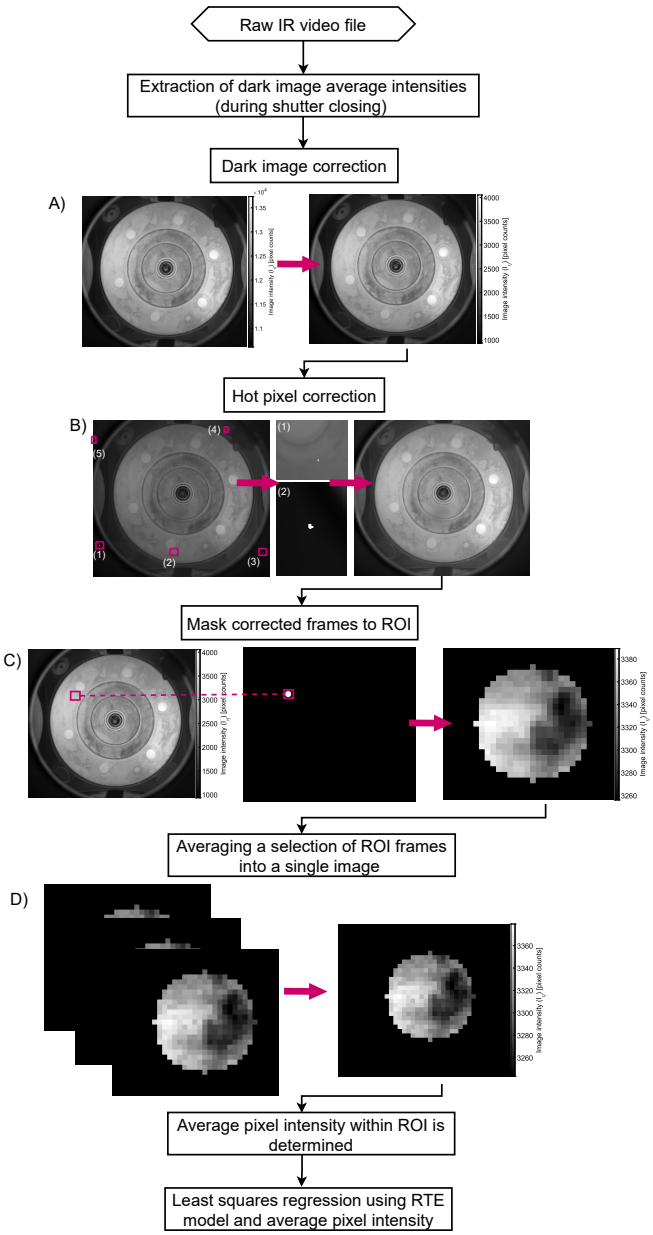

Figure 5: Image processing methodology flow chart for correcting raw IR video frames, masking procedure with ROI, averaging pixel intensities in ROI, and least squares model fitting with RTE equation. A) Subtraction of average image counts during shutter closing (non-uniformity correction). B) Correcting saturated pixels in red squares via replacing them by the average of neighbouring pixels. C) Corrected video file with ROI highlighted in red box. D) Masked frames are averaged into a single image which is then used for model fitting.

2.4. Solvents and experimental conditions/procedures

Two amine solvent mixtures were tested under flash boiling atomisation. The first was a 20:80 % w:w blend of triethanolamine ($C_6H_{15}NO_3$) and methanol (CH_3OH). Triethanolamine (TEA) was gas chromatography grade (Sigma-Aldrich, product number 90279), and contained ≤ 0.2 % water. Methanol was HPLC grade at ≥ 99.9 % purity, (Fisher Scientific, product number A4552-1). Isopropylamine (C_2H_9N) from Sigma-Aldrich (product number 471291) was gas chromatography grade (≥ 99.5 %) containing ≤ 0.1 % water. Isopropylamine (IPA) was selected as a primary amine over the industry standard of MEA (C_2H_7NO) due to its capability of fast kinetic reactions with CO_2 via the carbamate formation mechanism and its greater absorption capacity (Bernhardsen and Knuutila , 2017; Vega et al., 2018). TEA was mixed with methanol to keep the solvent blend boiling point as low as possible and minimise the energy penalty when desorbing CO_2 for solvent regeneration. The use of methanol instead of water decreased the boiling point of the blend by 19 %, from 147 °C to 119 °C. The gas cylinder used to fill the CV chamber with CO_2 during testing was research grade, with a purity of 99.999 %, and supplied by Matheson. Table 1 summarises the properties of the solvent mixtures and individual components.

Table 1: Solvent blend and component properties

	TEA	Methanol	TEA-methanol blend	IPA
CAS number	102-71-6	67-56-1	-	75-31-0
Critical temperature [°C]	508.99	240.25	294	198.65
Critical pressure [MPa]	4.32	8.22	7.44	4.54
Density [kg m^{-3}]	786.06	393	786.64	690
Boiling point [°C]	335.4	64.7	118.84	32

To simulate a degree of superheat for the flash boiling spray, several combinations of injector and chamber temperature conditions were tested for each solvent blend (Table 2). For the TEA solvent blend, conditions 1 to 3 followed a common gas temperature to isolate the effects of liquid temperature which are known to dictate the spray geometry, flash boiling regime, and spray characteristics such as droplet size distributions (Yang et al., 2016). Condition 4 involved raising the gas temperature whilst keeping solvent temperature common to one of the previous conditions to examine whether or not the temperature of the CO_2 has any significant effect on absorption.

This allowed for comparisons to be made whether liquid temperature or gas temperature had a more prevalent effect on overall capture performance. IPA has a significantly lower boiling point compared to TEA (Table 1) so solvent saturation pressures were not the same as the TEA mixture and a different set of temperature conditions were tested. Condition 5 was chosen to observe the capture performance at ambient conditions. To evaluate which amine solvent blend was more effective at CO_2 removal under similar conditions, CO_2 and solvent temperature for the IPA blend (condition 6) was matched with the TEA solvent mixture (condition 3). The vessel pressure was controlled by a pressure sensor installed within the chamber to ensure that the CO_2 was at atmospheric pressure before injecting any solvent for all temperature conditions. Equation 7 was used to quantify R_p as this directly relates the chemical potential difference that influences solvent phase transition, making it an accurate representation of superheat level (Lamanna et al., 2014). Vessel pressure was maintained at 0.1 MPa for all conditions to match gas pressures measured in typical gas scrubbing columns, thus variation in superheat was achieved by adjusting the solvent temperature and in turn its saturation pressure (p_{sat}).

$$R_p = \frac{p_{sat}}{p_{env}} \tag{7}$$

The test procedure began by purging the chamber with N_2 gas followed by heating the injector port via its PID temperature control system until the desired nozzle temperature was reached as detailed in Table 2. Once the injector port temperature was stabilised, videos were taken during this period for calibration and to set a reference point (at 0 % CO_2) for the RTE model image processing analysis since N_2 does not emit or absorb IR radiation at the observed wavelength. Afterwards, the N_2 gas was purged, and the chamber was filled with CO_2 until a chamber pressure of 0.1 MPa was reached. For some conditions this CO_2 filling period spanned two IR videos. The spray vessel and injector port were heated via independent PID temperature control systems until nozzle and gas temperatures reached the desired conditions (Table 2). Once the CO_2 and nozzle temperatures were stabilised, the solvent injection period began in which 8 separate videos, containing 4 solvent injections each, were recorded before the chamber was purged with N_2 at the end of the tests. During the solvent injection period, the gas inlet and outlet/purge valves remained shut thus no extra CO_2 was introduced or released from the system. The valves were electronically controlled and operated only at the beginning, during N_2 calibration and CO_2 filling, and end, following N_2 purging, of the testing procedure.

Table 2: Nozzle-chamber temperature conditions, vessel, and injection pressures used for testing. Flash boiling regimes of the sprays for each condition are listed in italic next to R_p values: Non/sub-cooled flash boiling (*Non-FB*), transitional flash boiling (*Trans FB*), Flare flash boiling (*Flare FB*)

Test condition	Solvent blend	Nozzle (solvent) temperature [°C]	Vessel (CO_2) temperature [°C]	Vessel pressure [MPa]	Injection pressure [MPa]	Total injected volume [mL]	R_p
60TEA60	TEA-MeOH	60	60	0.1	4	0.09	0.81 (*Non-FB*)
90TEA60	TEA-MeOH	90	60	0.1	4	0.09	2.73 (*Trans FB*)
120TEA60	TEA-MeOH	120	60	0.1	4	0.09	8.20 (*Flare FB*)
120TEA120	TEA-MeOH	120	120	0.1	4	0.08	8.20 (*Flare FB*)
60IPA20	IPA	60	20	0.1	4	0.43	2.49 (*Trans FB*)
120IPA60	IPA	120	60	0.1	4	0.31	11.23 (*Flare FB*)

3. Results and Discussion

3.1. Analysis of spray morphology

The degree of superheat (R_p) strongly influences the spray shape, distribution, and droplet size which can greatly impact CO_2 absorption. DBI snapshots of the spray side profile for each test condition and its evolution over a short time period are shown in Fig. 6 to assess spray morphology and potential implications for CO_2 capture performance. Using fixed global threshold binarization and knowing the digital resolution of the high-speed camera, the spray penetration at each condition was computed between 0 to 2 ms post first injection sequence and is displayed in Fig. 7. The spray angle and volume were computed between 0 to 1 ms post first injection and shown in Fig. 8 and 9, respectively. At low degrees of superheat ($R_p = 0.81$, non or minimal flash boiling) when $T_{TEA} = 60\,°C$ and $CO_2 = 60\,°C$ (Fig. 6C), the spray follows a typical conical shape with a larger spray cone angles (51 ° to 54 °), where the bulk of amine droplets are positioned near the injector centre line 1.1 ms after injection. The majority of the droplets quickly migrate toward the outer edge of the cone leaving the centre of the spray much less dense, indicated by the darker areas along the edges of the spray distribution, from 1.4 to 2 ms post injection. Over time, the conical spray pattern expands with the spray tips pushing further outwards towards the chamber walls further downstream (Fig. 6C), resulting in the largest spray volume of 18.6 mL 1 ms post first injection sequence (Fig. 9). However, due to the outward direction of the spray tips, the majority of these droplets were prone to colliding with, or impinging on, the chamber walls. When the degree of superheat is raised and solvent spray begins to follow the 'transitional' flash boiling regime ($1 < R_p < 3.33$), where $T_{TEA} = 90\,°C$, $T_{CO_2} = 60\,°C$, and $T_{IPA} = 60\,°C$,

T_{CO_2} = 20 °C (Fig. 6A and 6D), the spray shape changes significantly: the spray cone angle narrows to 37 ° (Fig. 6A and 8), and 38.8 ° (Fig. 6D) 0.6 ms post first injection sequence, whilst following a 'tulip' structure instead of the previous conical shape. The spray tips were observed to curl back towards the injector and are most obvious at the 1.7 and 2 ms mark for Fig. 6A and 6D. This is a common characteristic of flash boiled sprays caused by recirculation zones formed from aerodynamic interactions between the highly atomised droplets and surrounding CO_2 gas (Mojtabi et al., 2008; Zeng et al., 2012). These recirculation zones are advantageous as they increase the droplet residence time at the centre of the chamber and extend solvent-CO_2 contact to maximise absorption. Figs. 6B, 6E, and 6F display the sprays under the 'flare' flash boiling regime ($R_p > 3.33$) when solvent temperature is further increased to > 100 °C. At $T_{solvent}$ = 120 °C (Fig. 6B, E, F), the spray undergoes a complete collapse (spray cone angle ranging 17 ° to 30 °) where the majority of atomised droplets are localised near the injector centre axis creating a dense cloud (spray volume ranging from 6 to 9 mL in Fig. 9). This phenomenon can be beneficial for CO_2 spray tower applications as the inward or neutral spray direction ensures the majority of droplets are less prone to wall impingement and mitigate solvent losses which is a large drawback for widely or outward spraying atomisers (Seyboth et al., 2014; Cho et al., 2018). However, at very high droplet densities the likelihood of droplet coalescence increases and limits capture performance (Stolaroff et al., 2010; Chen et al., 2012), so a high spray density will not always improve CO_2 absorption. As superheat increases within the flare flash boiling regime (R_p from 8.20 to 11.23), spray density is observed to decrease as indicated by the lighter regions around the spray distribution in Fig. 6B compared to Fig. 6F. This is due to more of the highly atomised droplets undergoing vaporisation and is particularly evident in Fig. 6B as the IPA boiling point is significantly lower. Spray penetration is also observed to increase > 60 mm 1 ms after injection and span the whole length of the chamber after 1.8 ms (Fig. 7). These extended spray plumes can be beneficial as it increases surface area coverage length wise within the chamber over a shorter period of time, however too much can result in droplet impingement with the chamber walls. Increasing the gas temperature has no significant effect on the spray structure apart from a slight increase in the vaporisation of the solvent droplets as indicated by the slightly lighter regions at the 1.7 / 2 ms mark in Fig. 6F ($T_{solvent}$ = 120 °C) when compared to 6E ($T_{solvent}$ = 60 °C).

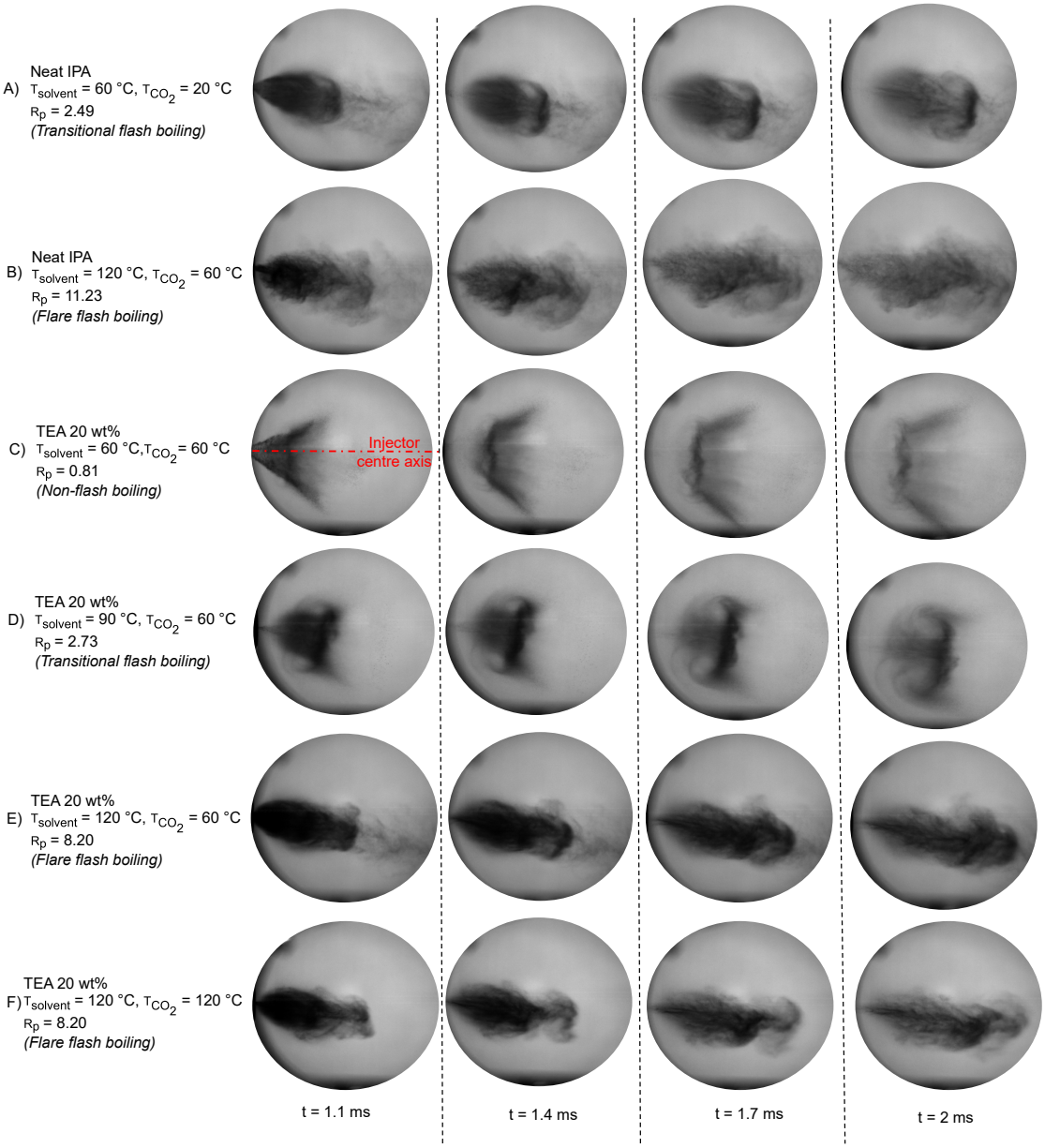

Figure 6: DBI snapshots of spray evolution after injection for all tested conditions and solvents.

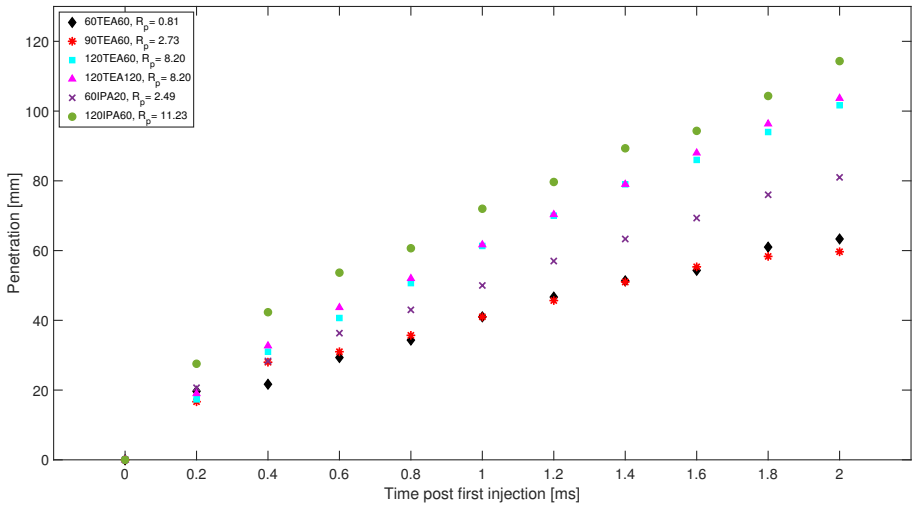

Figure 7: Spray penetration for each tested condition as a function of time

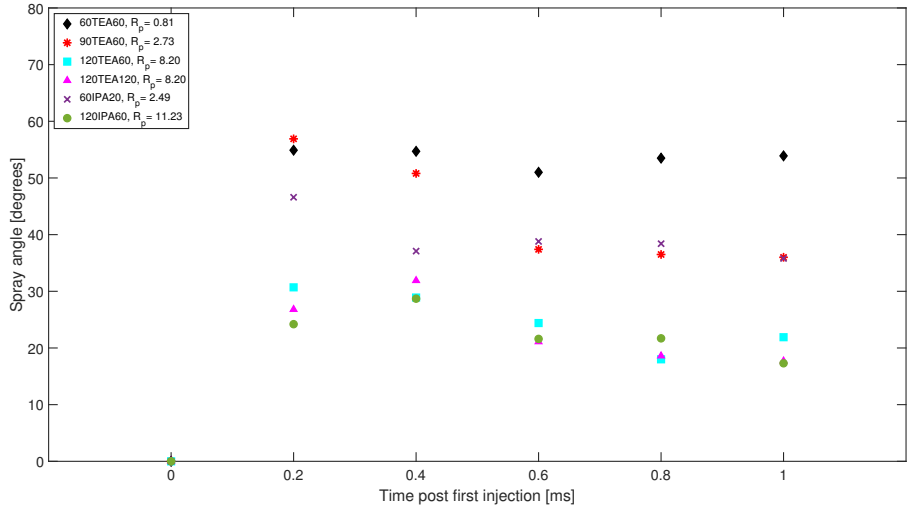

Figure 8: Spray angle for each tested condition as a function of time

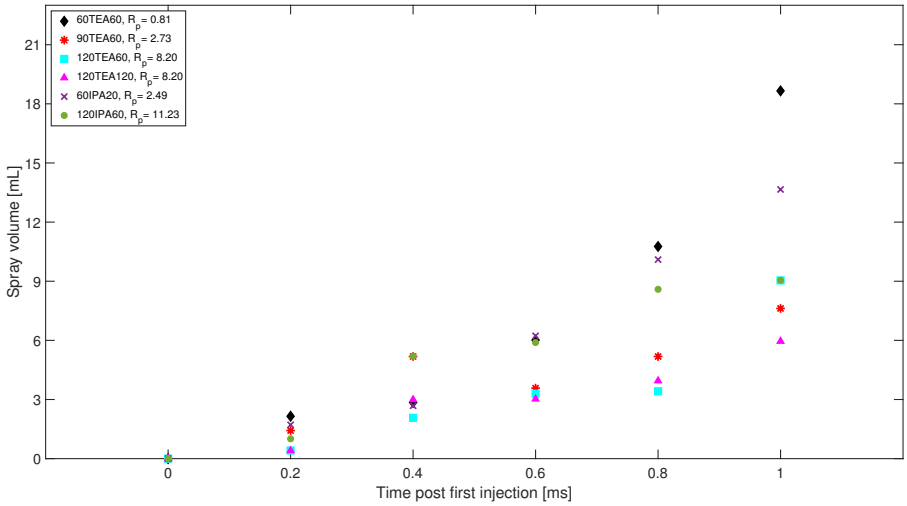

Figure 9: Estimated spray volume as a function of time, from start to end of injection. The spray volume was estimated from the spray angle and penetration length using a conical shape approximation.

3.2. Model results and uncertainty

3.2.1. Model reliability

The primary measurand for this work was the density of CO_2 post solvent injections (ρ_{CO_2}) which was calculated from the adapted RTE model (Equation 6). To determine the 'combined' standard uncertainty of the model predicted CO_2 density $\left(\frac{\delta_{\rho CO_2}}{\rho_{CO_2}}\right)$, Equation 8 was used:

$$\frac{\delta_{\rho CO_2}}{\rho_{CO_2}} = \sqrt{\left(\frac{\delta_{I_\eta}}{I_\eta}\right)^2 + \left(\frac{\delta_{I_{CO_{2,100}}}}{I_{CO_{2,100}}}\right)^2 + \left(\frac{\delta_{I_{\eta,0}}}{I_{\eta,0}}\right)^2 + \left(\frac{\delta_{\kappa_{\rho\eta}}}{\kappa_{\rho\eta}}\right)^2 + \left(\frac{\delta_{I_{b\eta}}}{I_{b\eta}}\right)^2 + \left(\frac{\delta_s}{s}\right)^2 + \left(\frac{\delta_{\rho_{CO_{2,100}}}}{\rho_{CO_{2,100}}}\right)^2} \tag{8}$$

where the standard uncertainties of each term in the modified RTE model (δ_{I_η}, $\delta_{I_{CO_{2,100}}}$, $\delta_{I_{\eta,0}}$, δ_{κ_η}, $\delta_{I_{b\eta}}$, δ_s, $\delta_{\rho_{CO_{2,100}}}$) were estimated using probability distribution functions and related instrument errors and uncertainties. More specifically, triangular distribution functions were applied to all reported instrument uncertainties to introduce a level of confidence in the measurements and convert them into 'standard' uncertainties. This involved dividing the listed uncertainties of relevant measuring devices by $\sqrt{6}$ to highlight that extreme values were unlikely, provided no confidence levels were already listed in the instrument specifications (Ellison and Williams, 2012). $\frac{\delta_{I_\eta}}{I_\eta}$ and $\frac{\delta_{I_{CO_{2,100}}}}{I_{CO_{2,100}}}$ were estimated by:

$$\frac{\delta_{I_\eta}}{I_\eta} = \frac{\delta_{I_{CO_{2,100}}}}{I_{CO_{2,100}}} = \sqrt{\left(\frac{\delta_{cam}}{cam}\right)^2 + \left(\frac{\delta_{P_{CO_2}}}{P_{CO_2}}\right)^2 + \left(\frac{\delta_{T_{noz,CO_2}}}{T_{noz,CO_2}}\right)^2} \tag{9}$$

where δ_{cam}, $\delta_{P_{CO_2}}$, and $\delta_{T_{noz,CO_2}}$ respectively correspond to the manufacturers' listed uncertainties of the IR camera, CO_2 pressure transducers, and PID temperature control system for the CO_2 and nozzle temperatures. These instruments significantly influenced the measured image intensities (I_η, $I_{CO_{2,100}}$) when the chamber was filled with CO_2. They were unlikely to report extreme values because the ROI used for the camera and image processing I_η was a small homogenous region containing no dead pixels ensuring little variation in pixel intensity values. Furthermore, the CV chamber was well sealed and the measuring components (pressure transducers) were routinely checked and maintained to prevent any leakages and significant drops in CO_2 pressure during tests. Finally, the PID system had a high accuracy sensor conformity ($\pm 0.1\%$ of calibrated temperature), and temperature gradients at the injector nozzle surface and CO_2 gas were minimal due to the use of six heating rods evenly heating the imaged area and an internal mixing fan maintaining gas uniformity. $\frac{\delta_{I_{\eta,0}}}{I_{\eta,0}}$ was estimated using:

$$\frac{\delta_{I_{\eta,0}}}{I_{\eta,0}} = \sqrt{\left(\frac{\delta_{cam}}{cam}\right)^2 + \left(\frac{\delta_{T_{noz}}}{T_{noz}}\right)^2} \tag{10}$$

The image intensity when the chamber was only filled with N_2 ($I_{\eta,0}$) was not affected by extra absorption or emission from the gas at the observed wavelength. Therefore, only the uncertainties of the camera (δ_{cam}) and PID system controlling the nozzle surface temperature ($\delta_{T_{noz}}$) impacted $I_{\eta,0}$. The uncertainty of CO_2 blackbody intensity ($\delta_{I_{b\eta}}$) was only dependent on the temperature of the gas ($\delta_{T_{CO_2}}$), which was equivalent to the PID temperature system uncertainty. The path length from heated injector surface to camera (s) was measured manually using a tape measure, hence its uncertainty was half of its smallest increment (0.5 mm) given it is an 'analog' measuring instrument (UKAS, 1997). $\frac{\delta_{\rho CO_{2,100}}}{\rho CO_{2,100}}$ was dependent on pressure, temperature, and purity of CO_2 and was estimated from:

$$\frac{\delta_{\rho CO_{2,100}}}{\rho CO_{2,100}} = \sqrt{\left(\frac{\delta_{P_{CO_2}}}{P_{CO_2}}\right)^2 + \left(\frac{\delta_{T_{CO_2}}}{T_{CO_2}}\right)^2 + \left(\frac{\delta_{CO_2,purity}}{CO_2,\,purity}\right)^2} \tag{11}$$

where $\delta_{CO_2,purity}$ is the uncertainty of the gas cylinder purity used for testing. As the gas bottle used was research grade quality with a listed purity of 99.999 %, large deviations in CO_2 concentrations were unlikely. The mass absorption coefficient ($\kappa_{\rho\eta}$) was influenced by CO_2 purity, temperature, pressure, path length, and intensity of radiation entering/leaving the CO_2, therefore $\frac{\delta_{\kappa\rho\eta}}{\kappa_{\rho\eta}}$ was estimated using:

$$\frac{\delta_{\kappa_{\rho\eta}}}{\kappa_{\rho\eta}} = \sqrt{\left(\frac{\delta_{P_{CO_2}}}{P_{CO_2}}\right)^2 + \left(\frac{\delta_{T_{CO_2}}}{T_{CO_2}}\right)^2 + \left(\frac{\delta_{I_\eta}}{I_\eta}\right)^2 + \left(\frac{\delta_{I_{\eta,0}}}{I_{\eta,0}}\right)^2 + \left(\frac{\delta_s}{s}\right)^2 + \left(\frac{\delta_{CO_2,purity}}{CO_2,\,purity}\right)^2} \tag{12}$$

As $k_{\rho\eta}$ is a calculated property (Equation 2), the uncertainties of δ_{I_η} and $\delta_{I_{\eta,0}}$ are propagated through in Equation 12. To assign a 95 % level of confidence to the 'combined' standard uncertainty of model predicted CO_2 $\left(\frac{\delta_{\rho CO_2}}{\rho CO_2}\right)$, a coverage factor ($k$) of 2 was used:

$$U_{\rho CO_2} = \left(\frac{\delta_{\rho CO_2}}{\rho CO_2}\right) k \tag{13}$$

where $U_{\rho CO_2}$ is the 'expanded' standard uncertainty of the model predicted CO_2 (ρCO_2).

3.2.2. Absorption capacity and molar absorption rate uncertainty

The expanded standard uncertainty of the calculated absorption capacity (U_x) and normalised molar absorption rate ($U_{k_{abs}}$) was determined using:

$$U_x = U_{k_{abs}} = k\sqrt{\left(\frac{\delta_{\rho CO_2}}{\rho_{CO_2}}\right)^2 + \left(\frac{\delta_{V_{inj,amine}}}{V_{inj,amine}}\right)^2} \tag{14}$$

where $\frac{\delta_{V_{inj,amine}}}{V_{inj,amine}}$ is the standard deviation of injected amine volume at each injection sequence and $\left(\frac{\delta_{\rho CO_2}}{\rho_{CO_2}}\right)$ is the propagated model predicted CO_2 uncertainty. Similar to section 3.2.1, a k of 2 was used giving the absorption capacity and molar absorption rate results an approximate level of confidence of 95 %.

3.2.3. Fitting results

The average signal intensity received by the camera at the specified region of interest was calculated for all IR recordings and conditions. Fig. 10 displays the average signal for $T_{TEA} = 120\,°C$, $T_{CO_2} = 60\,°C$ only where the signal intensity remains constant until CO_2 is introduced into the chamber (blue dashed line) which subsequentially cools the system. Between the end of the second CO_2 filling and first injection sequence recordings, the gas undergoes thermal stabilisation during which the cold CO_2 heats up to the temperature of the chamber. Therefore, the gas concentration during the pre-injection period of the first injection sequence and at the very end of the second CO_2 filling video remains constant, whilst intensity increases as a result of temperature and extra IR emission of the gas. Notably, the average signal intensity decreases directly after each solvent injection which is likely due to the solvent spray droplets undergoing evaporative cooling upon exposure to the hot CO_2. As the RTE model is dependent on signal intensity, averages were taken at the beginning of each injection sequence (pre-injection), where the gas is at local thermodynamic equilibrium, to avoid misleading predictions of CO_2 density. The timing between each injection sequence recording is irregular as the chamber required different lengths of time to thermally stabilise after each batch of solvent injections. The measured image intensities are presented with the modelled image intensities calculated from the RTE equation for all solvents and test conditions in Fig. 11A-F. With each injection sequence, the average intensity is observed to increase linearly which is linked to a reduction in CO_2 in the chamber over time. As the number of CO_2 molecules decreases within the chamber, less IR absorption from the gas occurs, permitting extra transmission of radiation emitted from the heated injector surface through to the camera sensor. The fitted I_η values calculated by the model fall within ± 1.5 % of the measured average intensities as displayed by the regression fitting residuals for each injection recording in Fig. 12. This indicates that the model accurately matches the experimental data.

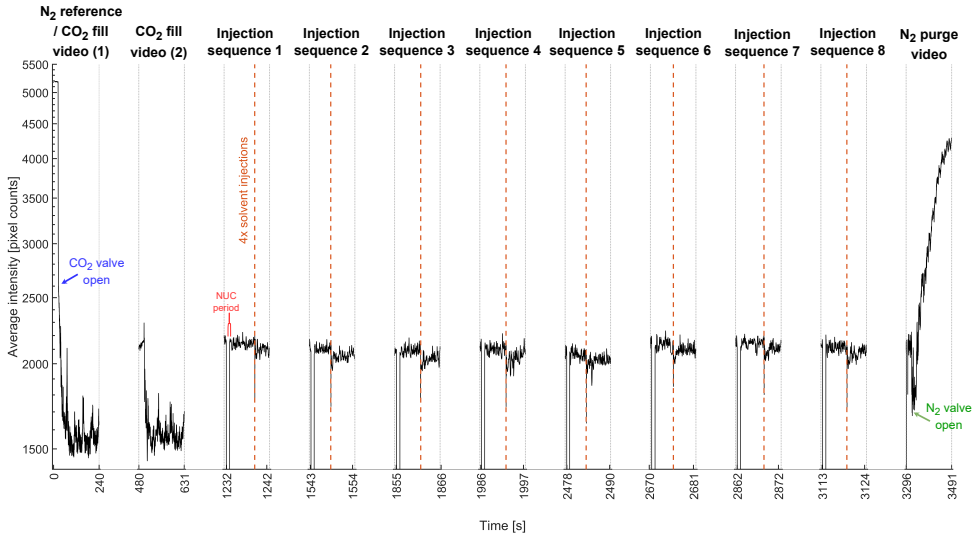

Figure 10: Non-uniformity corrected (NUC) average signal intensity within the masked ROI vs time for all recordings under the condition 120TEA60 ($T_{solvent}$ = 120 °C, T_{CO_2} = 60 °C) in order of experimental procedure from left to right. Injection of solvent in each recording is indicated by a vertical orange dashed lines.

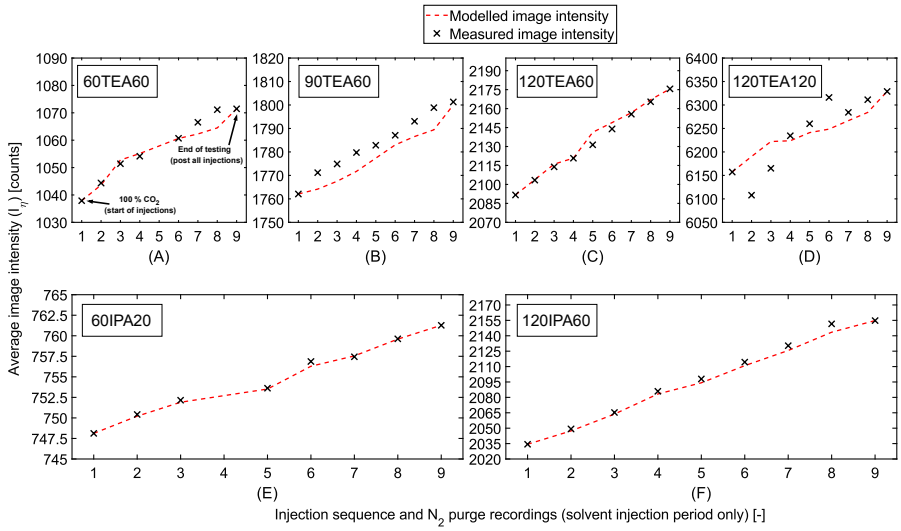

Figure 11: Measured and modelled image intensity vs injection sequence and N_2 purge IR recordings for conditions (A) T_{TEA} = 60 °C, T_{CO_2} = 60 °C, (B) T_{TEA} = 90 °C, T_{CO_2} = 60 °C, (C) T_{TEA} = 120 °C, T_{CO_2} = 60 °C, (D) T_{TEA} = 120 °C, T_{CO_2} = 120 °C, (E) T_{IPA} = 60 °C, T_{CO_2} = 60 °C, (F) T_{IPA} = 120 °C, T_{CO_2} = 60 °C

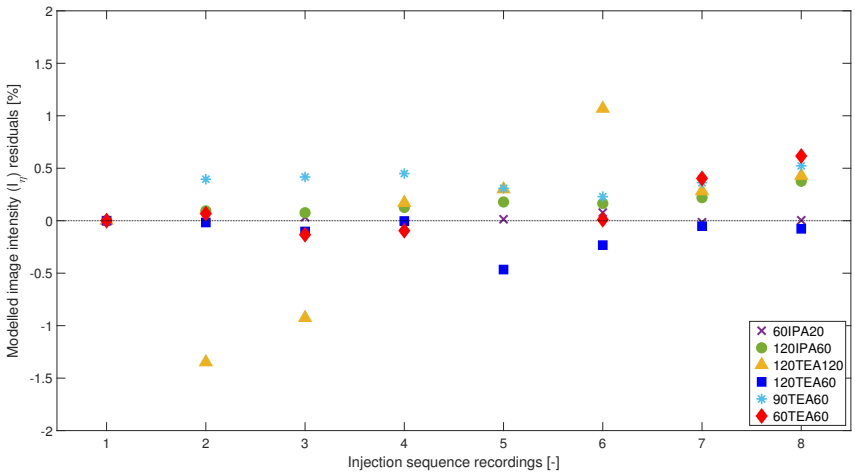

Figure 12: Image intensity residuals of the model post regression fitting with experimental signal intensities for all tested conditions.

Fig. 13 shows the predicted CO_2 densities at each injection sequence recording as a result of the regression fitting procedure and image processing methodology in Fig. 5 (section 2.3). The error bars correspond to the relative standard (expanded) uncertainty of the model from section 3.2.1 which was calculated to be at ± 2%. It can be seen that the CO_2 density drops with each injection sequence for all conditions and solvent blends, following an inverse relationship to the modelled image intensities (Fig. 11). The steeper decline in percentage of CO_2 at higher nozzle and gas temperature conditions suggest that operating at a spray regime with a higher degree of superheat results in greater CO_2 removal when compared to lower temperature conditions. In terms of total CO_2 absorption, the most effective temperature condition (120TEA120) is observed to only capture up to 15 % CO_2. Whilst this appears low, Fig. 13 does not take into account the number of moles of amine injected per sequence which can greatly impact perceived CO_2 removal. For this work, the total injected solvent volume for each recording was < 1 mL to shorten the injection period and minimise wear and damage on the sealing components of the atomiser. It is expected that when increasing the injected solvent volume per video, by increasing the length of injection period or introducing more injection batches, a greater amount of CO_2 removal will be observed. A fairer measure of the overall capture performance would be calculation of the absorption capacity and normalised molar absorption rate (subsection 3.4 which accounts for the absolute

amount of solvent injected relative to CO_2 absorption and differences in injected solvent amount due to instrumental uncertainties.

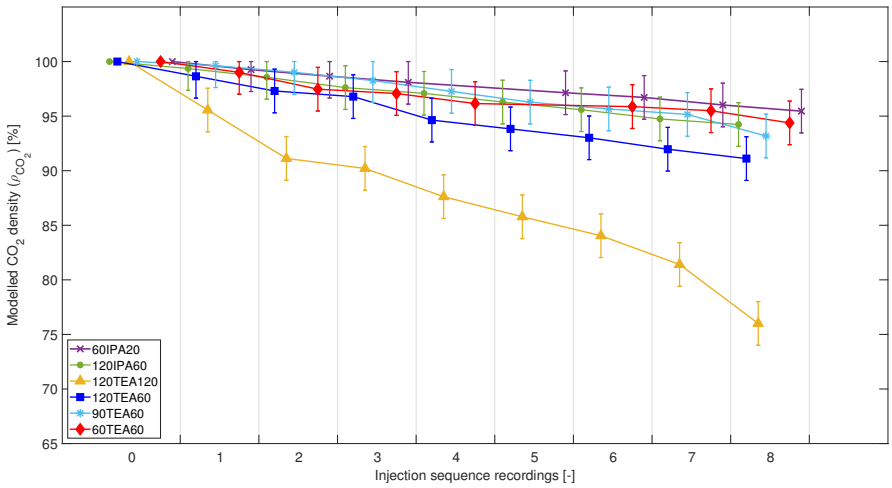

Figure 13: Model predicted CO_2 values from the beginning the test procedure to the final injection sequence recording.

3.3. *Temperature sensitivity of model*

A temperature sensitivity analysis was performed to examine how sensitive the RTE model was at predicting the quantity of CO_2 given an allowable nozzle and gas temperature deviation of $\pm 10\,^{\circ}C$. As the IR camera was setup to record injection videos in raw pixel data, the relationship between raw pixels and temperature was determined first. Based on the N_2 videos, which did not emit extra IR radiation in the observed spectral range, a change of 20.91 pixel counts corresponded to raising or decreasing temperature per 1 °C. The temperature sensitivity analysis was performed for three cases involving the change in temperature of nozzle only, gas only, and combined nozzle and gas. When adjusting the model to raise or decrease the nozzle temperature only by $\pm 10\,^{\circ}C$, 209.11 counts were added or subtracted to the input parameters (I_{η}, $I_{\eta,CO_2,100}$, $I_{\eta,0}$) impacted by nozzle temperature. The change in I_{η} meant that $I_{b\eta}$ had to be recalculated before regression fitting (section. 2.2) and predicting ρ_{CO_2}. For changing the gas temperature only, I_{η}, $I_{\eta,CO_2,100}$, and $I_{b\eta}$ were adjusted as stated previously, as the CO_2 temperature directly influences these parameters, whilst $I_{\eta,0}$ remained the same. New values for the theoretical density of CO_2 under 100% conditions ($\rho_{CO_2,100}$) were also selected at temperatures $\pm 10\,^{\circ}C$ from the original test points using NIST (Span and Wagner, 1996). When adjusting for both nozzle and gas temperature, the adjustments made to the RTE, previously described for changing nozzle and gas temperature individually, were combined resulting in modifying the following terms: I_{η}, $I_{\eta,0}$, $I_{\eta,CO_2,100}$, $I_{b,\eta}$, and $\rho_{CO_2,100}$. Fig. 14, 15, and 16 display the original modelled CO_2 densities (dashed lines and triangle or square data points) vs injection sequence when nozzle, gas, and combined nozzle and gas temperature are adjusted, respectively.

The dashed lines with triangular data points, as in Fig. 14A, 15A, and 16A, represent the IPA data set and the dashed lines with square data points, as in Fig. 14B, 15B, and 16B, represent the triethanolamine data set. The coloured shaded bands indicated the predicted CO_2 error when temperatures are $\pm 10\,^{\circ}C$ from the original test conditions. It was observed that the model was not sensitive to changes in nozzle temperature which had very little effect on predicted CO_2, with an error of $< 0.01\,kg\,m^{-3}$ for all test conditions. The model was more sensitive to changes in gas temperature as the predicted CO_2 error was larger, with the highest being $\pm 0.062\,kg\,m^{-3}$ for condition 60TEA60 in Fig. 15A. With a combined change in gas and nozzle temperature (Fig. 16), the total predicted CO_2 error increased marginally relative to those observed in Fig. 15. Overall, variation still remained insignificant at $< 0.07\,kg\,m^{-3}$ for all temperature conditions. The pre-

435 dicted CO_2 error decreased with each temperature condition in all cases which indicated that the
436 RTE model became less sensitive as the nozzle and gas temperature was increased.

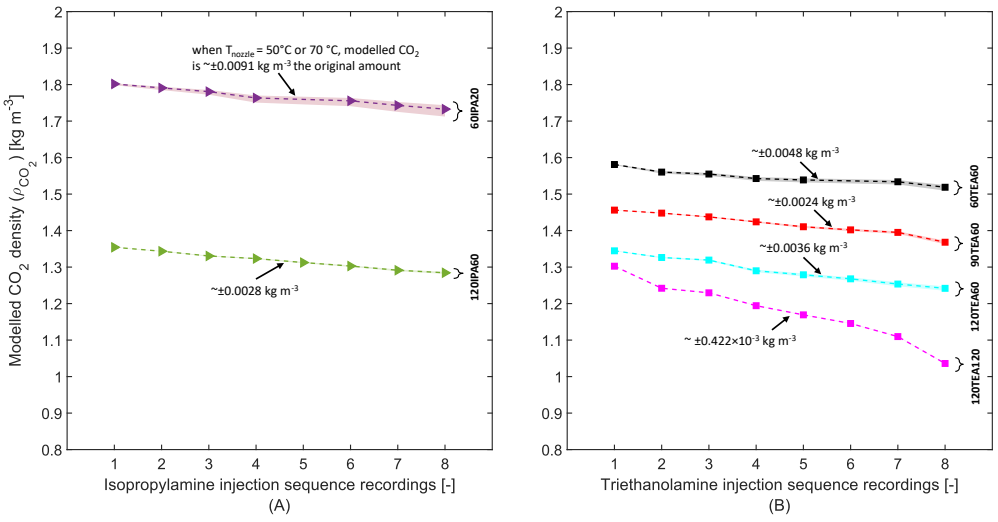

Figure 14: Temperature sensitivity analysis when only nozzle temperature is raised/decreased by ± 10 °C for the (A) Isopropylamine data set (B) Triethanolamine data.

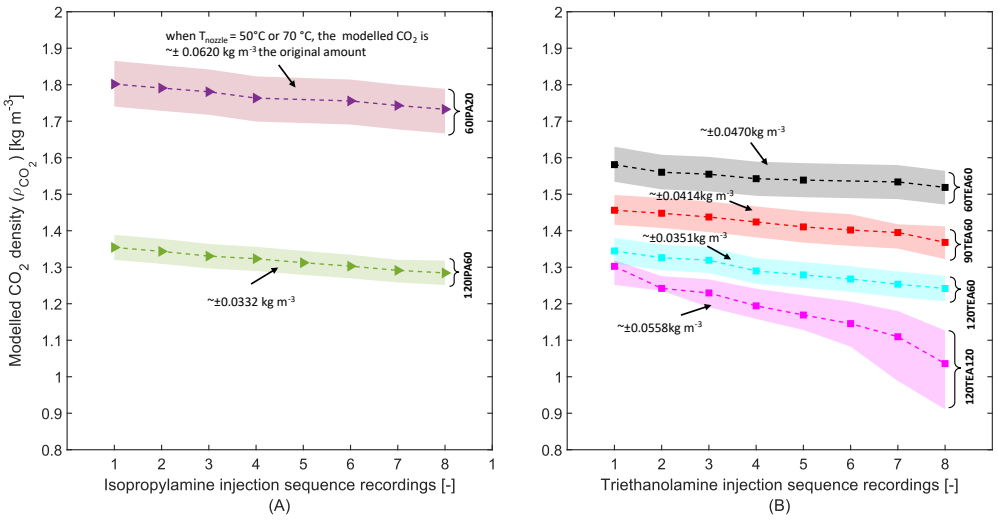

Figure 15: Temperature sensitivity analysis when only gas temperature is raised/decreased by ± 10 °C for the (A) Isopropylamine data set (B) Triethanolamine data.

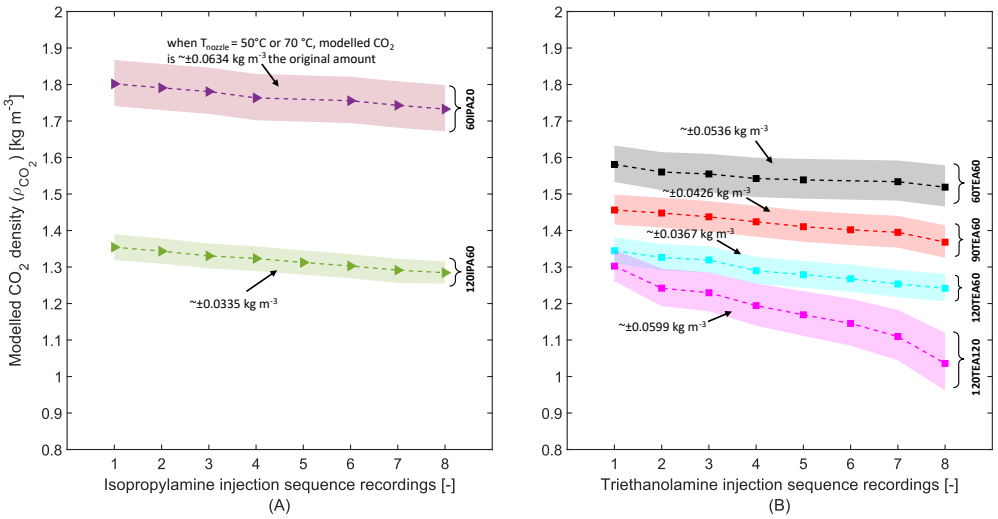

Figure 16: Temperature sensitivity analysis when both nozzle and gas temperature is raised/decreased by ± 10 °C for the (A) Isopropylamine data set (B) Triethanolamine data.

3.4. Effects of flash boiling regime on absorption capacity and molar absorption rate

The absorption capacity is calculated as:

$$x = \frac{n_{CO_2}}{n_{amine}} \tag{15}$$

Where x is the absorption capacity [$\mathrm{mol_{CO_2}/mol_{amine}}$], n_{CO_2} [mol] is the molar amount of CO_2 absorbed, and n_{amine} [mol] is the total amount of amine present in the chamber. In this analysis, absorption capacity was calculated between each injection sequence, hence n_{CO_2} was based on CO_2 absorbed between each recording. n_{amine} was calculated as the cumulative sum of individual injections at each sequence because the chamber remained closed throughout testing and was not purged after each recording. With each solvent injection, the number of amine molecules within the chamber built up steadily and continued to absorb until saturation. This was unlike typical spray or packed column absorption towers where the solvent within the column remains relatively constant, assuming a fixed flow rate, as it is immediately cycled out for regeneration after reaching the bottom. The molar absorption rate is calculated using:

$$k_{abs} = \frac{n_{CO_2}}{t_{exp}} \tag{16}$$

where k_{abs} is the absorption rate [mol_{CO_2}/mol_{amine}] and t_{exp} [seconds] is the time period of solvent exposure to the CO_2 (contact time). Contact time was calculated based on the duration between the moment of solvent injection and time corresponding to the set of video frames chosen for image processing and model fitting to predict CO_2 density (section 2.3). As the volume of solvent for each injection sequence varied due to instrumental variance and impacted CO_2 absorption, Equation 16 was modified such that the amount of CO_2 absorbed was divided further by the number of moles of amine present in the chamber:

$$k'_{abs} = \frac{n_{CO_2}}{t_{exp} n_{amine}} \tag{17}$$

to give a normalised absorption rate (k'_{abs}) [mol mol^{-1} s^{-1}] indicating the moles of CO_2 absorbed per mol of amine per second.

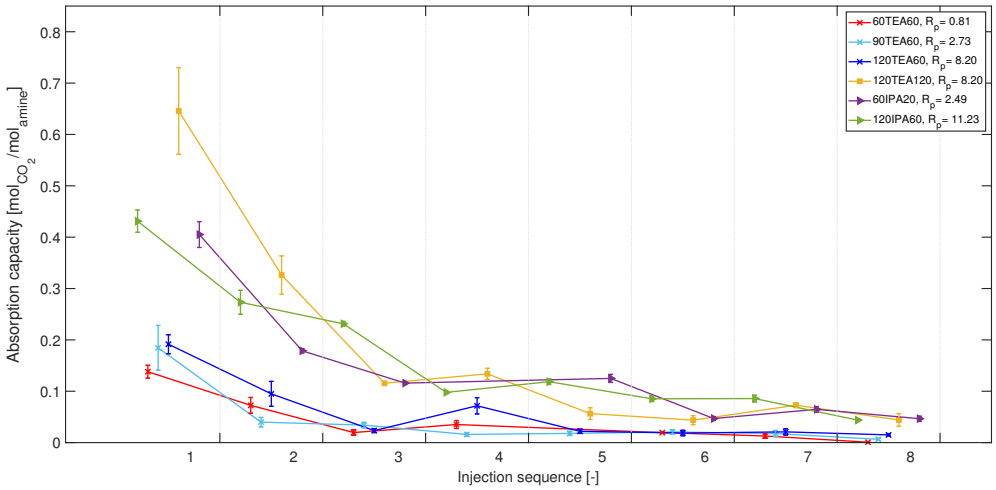

Figure 17: Absorption capacity vs injection sequence for each temperature condition and amine tested. Error bars represent the expanded standard uncertainties of absorption capacity at each injection sequence.

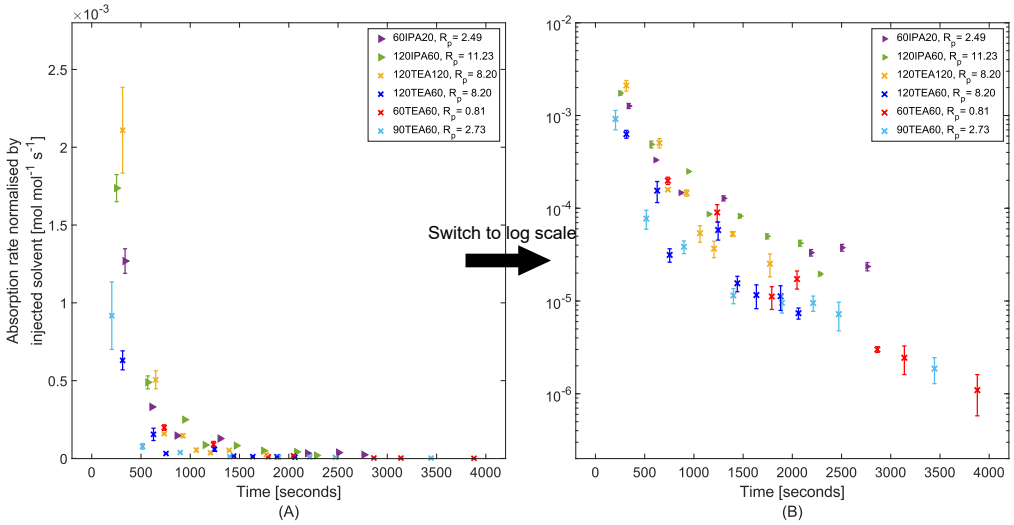

Figure 18: Absorption rate normalised for injected solvent at each injection sequence vs time. A) Absorption rate in a linear scale vs time. B) Absorption rate in log scale vs time. Error bars represent the expanded uncertainties of molar absorption rate at each injection sequence.

Fig. 17 displays the calculated absorption capacities for all tested temperature conditions and solvents at each injection sequence recording. Fig. 18 displays the normalised molar absorption rate against time on a linear (Fig. 18A) and logarithmic scale (Fig. 18B). Test conditions where the nozzle and chamber were heated to high temperatures, e.g. 120TEA120, 120TEA60, 120IPA60, required less time between each injection sequence to restabilise to the appropriate test conditions and had a shorter overall test period (up to 2500 s), as opposed to lower temperature test conditions, e.g. 60TEA60, 60IPA20, 90TEA60 (up to 4000 s as seen on Fig 18). The error bars represent the expanded standard uncertainty of absorption capacities and molar absorption rates, calculated using Equation 14 at each injection sequence. The largest uncertainty being $\pm\,0.08\,\mathrm{mol_{CO_2}}\,/\,\mathrm{mol_{amine}}$ (Fig. 17) and $\pm\,0.28\times10^{-3}$ mol mol^{-1} s^{-1} (Fig. 18) during the first set of injections for condition 120TEA120. This was due to variations in injected volume during this sequence as a result of rapid liquid boiling causing fluctuating injection pressures. With a cumulative build-up of amine molecules in the chamber a continuous increase in absorption could be expected due to more reactant being present. Contrary to this, capture performance and absorption rate was observed to drop significantly after the first injection sequence and further decrease as more TEA and IPA were introduced into the chamber in Fig. 17 and 18. The

molar absorption rate followed an exponential decay with time in Fig. 18A, which decreased linearly when converting to a logarithmic scale (Fig. 18B), suggesting that the chemical reaction occurring between the CO_2 and TEA/IPA was a first order reaction. As the gradient of CO_2 concentration at the gas-liquid interface on the droplet surface is reduced over time, due to absorption from previous injection sequences, the resulting driving force for mass transfer is smaller leading to a slower chemical reaction (Doran, 1995). This effect was not obvious when observing the modelled CO_2 densities (Fig. 13). Decrease in CO_2 concentration from first to last injection sequences appeared minimal due to the small amount of solvent injected (< 1 mL), hence this process occurred at a significantly smaller scale. The absorption capacity and molar absorption rate for all temperature conditions was highest after the first injection sequence since the solvent was exposed to the CO_2 at its highest concentration during this period, promoting a steeper gradient at the gas-liquid interface and faster reaction/absorption process. Conditions during the first injection sequence most resemble those in typical spray towers where the solvent spray is exposed to a continuous feed of flue gas. Therefore, the focus of the following discussions on absorption capacities and molar absorption rates will be on comparing results specifically at the first injection sequence.

3.4.1. Non/sub-cooled flash boiling regime

When operating at a lower R_p and temperatures, capture performance appeared to be much less effective. At $T_{TEA} = 60\,°C$ and $T_{CO_2} = 60\,°C$ (60TEA60), the absorption capacities were calculated to be the lowest, at $0.138\,mol_{CO_2}\,/\,mol_{amine}$ after the first injection sequence recording down to $0.001\,mol_{CO_2}\,/\,mol_{amine}$ after the last (Fig. 17). This corresponds directly with the calculated molar absorption rate at the same temperature condition, at 0.20×10^{-3} mol mol^{-1} s^{-1} post first injection sequence (contact time of 735 s), which was the slowest out of all tested temperature conditions. Larger droplet sizes, typically as a result of lower R_p value (as observed in Zeng et al. (2012); Cleary et al. (2007); Witlox et al. (2007)) are likely the reason why the absorption rate at condition $T_{amine} = 60\,°C$ and $T_{CO_2} = 60\,°C$ was the slowest.

3.4.2. Transitional flash boiling regime

When $T_{TEA} = 90\,°C$ (90TEA60) and $R_p = 2.73$, absorption capacity after the first injection sequence increased to $0.185\,mol_{CO_2}\,/\,mol_{amine}$, equivalent to a 34 % boost in capture performance compared to the non flash boiled TEA solvent spray. This is directly linked to the substantial

improvement of molar absorption rate which was observed to increase by a factor of 4.5 despite having a shorter droplet contact time (0.91×10^{-3} mol mol^{-1} s^{-1} at 203.8 s). From this, it is clear that the spray characteristics formed when operating under the transitional regime (e.g. smaller droplet sizes, wider spray angle, droplet recirculation zones) as explained in section 3.1 are more favourable for CO_2 absorption compared to the non flash boiled spray. The absorption capacity of the IPA solvent spray when $T_{amine} = 60\,°C$ and $T_{CO_2} = 20\,°C$ (60IPA20) under the transitional flash boiling regime was 0.41 mol_{CO_2} / mol_{amine} post first injection sequence which is approaching the theoretical capacity limit of this type of amine at 0.5 mol_{CO_2} / mol_{amine}. This corresponds to a molar absorption rate of 1.2×10^{-3} mol mol^{-1} s^{-1} at a 338.6 s droplet contact time.

3.4.3. Flare flash boiling regime

When raising T_{TEA} from 90 °C to 120 °C to operate under the flare flash boiling regime ($R_p = 8.20$), the calculated absorption capacity and molar absorption rates post first injection sequence were raised further to 0.192 mol_{CO_2} / mol_{amine} and 0.63×10^{-3} mol mol^{-1} s^{-1} (at a 252 s contact time), respectively. Interestingly, the improvement of capture performance when increasing T_{TEA} from 60 to 90 °C was much more prominent, a 34 % increase compared to the marginal 4 % improvement observed when T_{TEA} was raised from 90 to 120 °C. This same trend was observed with absorption rates, whereby molar absorption rates increased by only 3x from non to flare flash boiling regime, as opposed to the 4.5x boost from non to transitional flash boiling. This was most likely linked to the change in spray properties at $T_{TEA} = 120\,°C$ due to the spray collapse phenomena, as described in section 3.1. More specifically, the increase in R_p promoted atomisation of the solvent into smaller droplet diameters, however, the resulting collapsed denser spray distribution increased susceptibility to droplet coalescence which negated the total benefits this type of spray provided. For the case of IPA solvent spray, a similar marginal increase capture performance was observed when moving from a transitional to flare flash boiling regime via raising T_{IPA} from 60 °C to 120 °C (0.405 to 0.431 mol_{CO_2} / mol_{amine}), which was equivalent to only a 6 % improvement in absorption capacity.

3.5. Effects of gas temperature on absorption capacity and molar absorption rate

When increasing T_{CO_2} from 60 °C to 120 °C whilst maintaining a constant solvent temperature (120TEA60 to 120TEA120), capture performance improved drastically from an initial 0.192 to 0.646 mol_{CO_2} / mol_{amine} after the first injection sequence. The speed of absorption was greatly

improved, where the molar absorption rate increased by a factor of 3.3 from an initial 0.63×10^{-3} to 2.1×10^{-3} mol mol^{-1} s^{-1} at a 313 s droplet contact time. This improved capture rate was likely caused by excitation of CO_2 molecules within the chamber at elevated temperatures enhancing the diffusive coefficient and mixing with the liquid amine promoting a faster chemical reaction (Chen et al., 2013; Ahmadi et al., 2020; Versteeg et al., 1996). With a higher diffusion coefficient, more CO_2 molecules were able to penetrate and fully saturate the solvent droplets hence the capture performance at 120TEA120 was significantly higher than 120TEA60 despite having similar spray structures (Fig. 6F and 6G).

3.6. Relationship between total absorption capacity and flash boiling regime

The total absorption capacity is a representation of the capture performance across all injection sequence recordings as opposed to specifically between each video as discussed in subsection 3.4. It is calculated by:

$$y = \frac{\sum_{i=1}^{8} n_{CO_2}}{(n_{amine})_{i=8}} \tag{18}$$

where y is the "total" absorption capacity [mol_{CO_2}/mol_{amine}] and i is the injection sequence recording number. As explained in section 3.4, n_{amine} is the cumulative sum of individual injections; Therefore to get the total absorption capacity across all recordings, the sum of moles absorbed at each sequence is divided by the total number of moles present within the chamber which is calculated after the final injection sequence ($(n_{amine})_{i=8}$). Fig. 19 displays the calculated total absorption capacity for each solvent against R_p segmented into the specific flash boiling regimes. It is clear that an increase in the degree of superheat leads to improved capture performance. At an R_p of 0.81, the TEA-methanol solvent blend achieved a total absorption capacity of 0.08 mol_{CO_2} / mol_{amine} which was raised to 0.11 mol_{CO_2} / mol_{amine} (a 28 % improvement) when R_p was increased to 2.73. When raising R_p to 8.20 from 2.73, a greater increase in capture performance was observed and the total absorption capacity was boosted to 0.16 mol_{CO_2} / mol_{amine} (a 44% improvement). This contradicts what was discussed in section 3.4.3 where there was a greater improvement when R_p was raised from 0.81 to 2.73 (T_{amine} from 60 to 90 °C) as opposed to increasing R_p from 2.73 to 8.20 (T_{amine} from 90 to 120 °C). This is due to the TEA-methanol spray within the flare regime (120TEA60) still maintaining an equal or higher absorption capacity (x) for most injection sequence recordings (Fig. 17) relative to the lower R_p sprays (60TEA60

and 90TEA60). For the IPA solvent, the total absorption capacity improved by 33% (0.37 to 0.50 mol_{CO_2} / mol_{amine}) when raising R_p from 2.49 to 11.23. It is important to note that *y* takes into account the decline in absorption and capture performance after the first injection sequence recording, which is why these values appear lower than the absorption capacity post first injection sequence discussed in section 3.4.

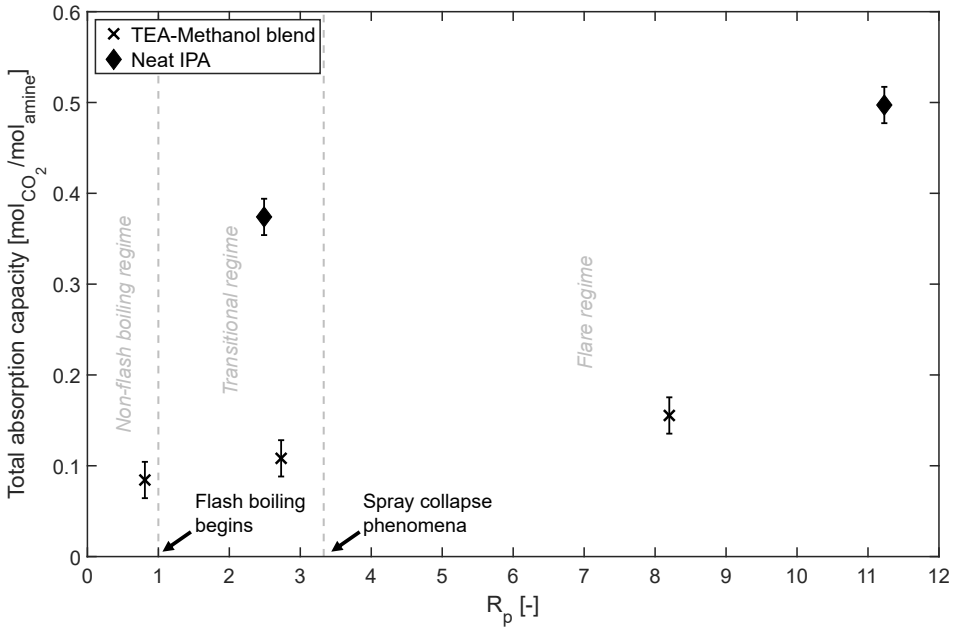

Figure 19: Total absorption capacity vs R_p for the tested TEA-methanol and neat IPA solvents

In summary, operating at a spray regime with high degrees of superheat and greater gas temperatures enhanced absorption speed and improved capture performance for a variety of solvent types, e.g. non-aqueous amine blends, primary, and tertiary amines. Enhancement of the molar absorption rate via superheated flash boiled sprays make slower reacting solvents, e.g. tertiary amine types such as triethanolamine, viable for use in spray columns. Furthermore, operational and manufacture costs can potentially be minimised as faster absorption rates permit use of shorter spray columns as a result of efficient capture performance under shorter droplet contact times. However, careful selection of which flash boiling regime and the magnitude of R_p to operate in is required. Whilst increasing R_p may initially boost capture performance significantly, particularly when in the transitional flash boiling regime, increasing into the flare flash

boiling regime may introduce some unfavourable spray properties, e.g. droplet coalescence, that may diminish the overall benefits this atomisation method provides. Furthermore, there are several key disadvantages associated with the flash boiling atomisation method to be considered before implementing this for large scale CO_2 capture applications: Whilst boiling of the solvent is advantageous in aiding the liquid break-up process by creating fine and uniform droplets, a portion of the solvent is lost in vapour form which may reduce the efficiency of the system when considering a cyclic process. Release of the vaporised amines lost from the flash boiling process into the environment may be harmful for any nearby humans and wildlife (secondary pollution), although this can be mitigated through the use of solvent recovery auxiliary systems which aim to condense/recuperate any evaporated amines. Additionally, as mentioned in section 1, smaller droplets created by flash boiled sprays are prone to getting entrained in the gas flow and impinging the column walls resulting in significant solvent losses, therefore requiring alternative designs for larger scale CO_2 capture systems that deal with faster flowing and large volumes of flue gas. Finally, the high injection pressures required to trigger the flash boiling phenomena, such as the 4 MPa used for the solvent blends tested in this work, demands vast energy consumption making this particular atomisation method less economical to implement commercially. Although, flash boiling atomisation may also be achieved via decreasing the ambient gas pressure in the chamber such that it falls underneath the saturation pressure of the solvent blend, removing the need for high injection pressures to trigger spray boiling/break-up and therefore alleviating the energy penalty; This specific method will require a significant reduction in partial pressure of CO_2 in the chamber which may hinder the overall capture performance of the spray. Adjusting ambient back pressure of the CO_2 in the chamber and injection pressures to control flash boiling remains open for exploration for future studies. The flash boiling atomisation method presents a number of advantages and disadvantages, and further investigation is required before this system can be implemented commercially and at scale. Nonetheless, the present study shows that varying superheat when flash boiling solvent blends is a viable mechanism for fine control of spray properties and efficient CO_2 absorption.

4. Conclusions

In this article we proposed for the first time that exploiting the physics of flash boiling sprays could improve spray carbon capture performance, and demonstrated that high degrees of superheat can indeed significantly improve the absorption rate and absorption capacity of amine solvent blends.

A model developed to quantify CO_2 densities from the IR recordings was evaluated to have reasonable accuracy ($\pm$ 1.5%), minimal uncertainty (relative standard uncertainty of $\pm$ 2 %), and low sensitivity to deviation in nozzle/gas temperature ($< 0.07\,\mathrm{kg\,m^{-3}}$). Superheat was achieved through heating the solvent blends to temperatures between 60 to 120 °C. The DBI extinction imaging technique successfully captured temporal spray characteristics and verified the occurrence of flash boiling and distinct spray regimes. Absorption capacities and molar absorption rates were calculated for each set of test conditions based on a radiative heat transfer model fitted to the optical experimental data. The effectiveness of increasing superheat on CO_2-absorbing flash boiling sprays was demonstrated for the first time. The main conclusions are:

1. Absorption capacity increases of 34 % and 6 % were observed for the methanol TEA and IPA solvents, respectively.
2. Greater improvement in absorption capacity was observed when R_p was increased from an initial 0.81 to 2.73, in the transitional flash boiling spray regime, as opposed to 8.2, in the flare flash boiling spray regime, suggesting possible diminishing returns in capture performance with solvent temperature.
3. Increasing the environment (CO_2) temperature, e.g. $T_{CO_2} = 60$ to 120 °C for 120TEA60 to 120TEA120, greatly improved the absorption capacity and molar absorption rate of the methanol TEA blend by a factor of 3.3.
4. The molar absorption rate was observed to increase by a factor of 4.5 for the non-aqueous TEA blend when R_p was raised from 0.81 to 2.73.

Future investigations of flash boiling carbon capture could focus on adjusting the type of atomiser and analysing how spray parameters, e.g. mono-dispersity, mean droplet size, or droplet velocity, impact capture performance remains an open avenue for exploration, as it has been established that the atomiser geometry can influence the flash regime and spray structure. Other methods of triggering flash boiling such as the adjustment of injection and ambient chamber pressure have

yet to be studied in the context of CO_2 capture and may present unique benefits. Furthermore, the effects of varying the CO_2 flow field on absorption performance whilst using flash boiling atomisation is another topic to be investigated before this method can be considered for application in commercial spray tower systems.

5. Abbreviations

MWIR: Mid-wave infrared.

RTE : Radiative heat transfer equation.

TEA: Triethanolamine.

IPA: Isopropylamine.

6. Acknowledgements

The authors would like to thank Kyra Schmidt at Sandia National Laboratories for her dedicated support of the Spray Laboratory. The optical measurements were performed at Sandia National Laboratories in Livermore, CA. Sandia is a multi-mission laboratory managed and operated by National Technology and Engineering Solutions of Sandia, LLC., a wholly owned subsidiary of Honeywell International, Inc., for the U.S. Department of Energy's National Nuclear Security Administration under contract DE-621 NA000352. Sincere thanks are extended to the University of Brighton. This work was supported by the University of Brighton in collaboration with University Alliance as part of the Doctoral Training Alliance 'Future Societies' programme.

7. Author Contributions: CRediT statement

Louis Dacanay: Formal analysis, Methodology, Visualisation, Writing - Original Draft, Conceptualization, Software, Data curation. **Kevin Wan**: Investigation, Resources, Writing - Review & Editing. **Julien Manin**: Investigation, Resources, Funding acquisition, Writing - Review & Editing. **Guillaume De Sercey**: Software, Writing - Review & Editing. **Peter J. Cragg**: Writing - Review & Editing. **Alain Ledoux**: Writing - Review & Editing. **Lionel Estel**: Writing - Review & Editing. **Cyril Crua**: Conceptualization, Investigation, Data Curation, Supervision, Project administration, Funding acquisition, Writing - Review & Editing, Software.

8. Funding sources

This research is funded by the University of Brighton and the University Alliance as part of the Doctoral Training Alliance 'Future Societies' programme.

References

Adeosun, A., and Abu-Zahra, M.R., 2013. Evaluation of amine-blend solvent systems for CO_2 post-combustion capture applications, *Energy procedia*, 37, pp. 211-218. DOI: 10/j98x

Ahmadi, H., Jamialahmadi, M., Soulgani, B.S., Dinarvand, N., and Sharafi, M.S., 2020. Experimental study and modelling on diffusion coefficient of CO_2 in water, *Fluid Phase Equilibria*, 523,pp. 112584. DOI: 10/gjpz7n

Aori, G., Hung, D.L., Zhang, M., Zhang, G. and Li, T., 2016. Effect of nozzle configuration on macroscopic spray characteristics of multi-hole fuel injectors under superheated conditions. *Atomization and sprays*, 26(5). DOI: 10.1615/AtomizSpr.2015011990.

Bernhardsen, I.M. and Knuutila, H.K., 2017. A review of potential amine solvents for CO_2 absorption process: Absorption capacity, cyclic capacity and pKa. *International Journal of Greenhouse Gas Control*, 61, pp.27-48. DOI: 10.1016/j.ijggc.2017.03.021.

Biliyok, C., Lawal, A., Wang, M., and Seibert, F, 2012. Dynamic modelling, validation and analysis of post-combustion chemical absorption CO_2 capture plant. *International Journal of Greenhouse Gas Control*, 9, pp. 428-445. DOI: 10/f36f4v

Chen, W.H., Hou, Y.L. and Hung, C.I., 2012. Influence of droplet mutual interaction on carbon dioxide capture process in sprays. *Applied energy*, 92, pp.185-193. DOI: 10.1016/j.apenergy.2011.10.035.

Chen, W.H., Chen, S.M. and Hung, C.I., 2013. Carbon dioxide capture by single droplet using Selexol, Rectisol and water as absorbents: A theoretical approach. Applied energy, 111, pp.731-741. DOI: 10.1016/j.apenergy.2013.05.051.

Cho, M., Lee, S., Choi, M. and Lee, J.W., 2018. Novel spray tower for CO2 capture using uniform spray of monosized absorbent droplets. *Industrial & Engineering Chemistry Research*, 57(8), pp.3065-3075. DOI: 10.1021/acs.iecr.7b05309.

Cleary, V., Bowen, P. and Witlox, H., 2007. Flashing liquid jets and two-phase droplet dispersion: I. Experiments for derivation of droplet atomisation correlations. *Journal of hazardous materials*, 142(3), pp.786-796. DOI: 10.1016/j.jhazmat.2006.06.125.

Doran, P.M., 1995. *Bioprocess engineering principles*. Elsevier.

El Hadri, N., Quang, D.V., Goetheer, E.L. and Zahra, M.R.A., 2017. Aqueous amine solution characterization for post-combustion CO_2 capture process. *Applied Energy*, 185, pp.1433-1449. DOI: 10/gpqwqf

Ellison, S.L. and Williams, A., 2012. Quantifying uncertainty in analytical measurement.

Environment Agency, Post-combustion carbon dioxide capture: best available techniques (BAT), accessed October 18th 2022, from: www.gov.uk

Gaur, A., Saha, K. and Ghai, D.P., 2024. Experimental characterization of early, quasi-steady and post-injection evolution of single-hole direct injection sprays for spark-ignited engines. *Thermal Science and Engineering Progress*, 47, p.102270. DOI: 10.1016/j.tsep.2023.102270.

Guo, H., Li, C., Shi, X., Li, H. and Shen, S., 2019. Nonaqueous amine-based absorbents for energy efficient CO_2 capture. *Applied energy*, 239, pp.725-734. DOI: 10.1016/j.apenergy.2019.02.019.

Gupta, M., Coyle, I. and Thambimuthu, K., 2003, September. CO_2 capture technologies and opportunities in Canada. In 1st Canadian CC&S Technology Roadmap Workshop (Vol. 18, p. 19).

Hwang, J., Kim, J., Lee, H.W., Na, J., Ahn, B.S., Lee, S.D., Kim, H.S., Lee, H. and Lee, U., 2019. An experimental

based optimization of a novel water lean amine solvent for post combustion CO_2 capture process. *Applied energy*, 248, pp.174-184. DOI: 10.1016/j.apenergy.2019.04.135.

Javed, K.H., Mahmud, T. and Purba, E., 2010. The CO_2 capture performance of a high-intensity vortex spray scrubber. *Chemical Engineering Journal*, 162(2), pp.448-456. DOI: 10.1016/j.cej.2010.03.038.

Kapusta, Ł.J., 2022. Understanding the collapse of flash-boiling sprays formed by multi-hole injectors operating at low injection pressures. *Energy*, 247, p.123388. DOI: 10.1016/j.energy.2022.123388.

Kavoshi, L., Rahimi, A. and Hatamipour, M.S., 2015. CFD modeling and experimental study of carbon dioxide removal in a lab-scale spray dryer. *Chemical Engineering Research and Design*, 98, pp.157-167. DOI: 10.1016/j.cherd.2015.04.023.

Kohl, A. L., and Nielsen, R., *Gas purification*, Elsevier, pp. 6-35, 1997.

Kuntz, J. and Aroonwilas, A., 2009. Mass-transfer efficiency of a spray column for CO_2 capture by MEA. *Energy Procedia*, 1(1), pp.205-209. DOI: 10.1016/j.egypro.2009.01.029.

Lai, Q., Kong, L., Gong, W., Russell, A.G. and Fan, M., 2019. Low-energy-consumption and environmentally friendly CO_2 capture via blending alcohols into amine solution. *Applied Energy*, 254, p.113696. DOI: 10.1016/j.apenergy.2019.113696.

Lamanna, G., Kamoun, H., Weigand, B. and Steelant, J., 2014. Towards a unified treatment of fully flashing sprays. *International Journal of Multiphase Flow*, 58, pp.168-184. DOI: 10.1016/j.ijmultiphaseflow.2013.08.010.

Li, K., Leigh, W., Feron, P., Yu, H. and Tade, M., 2016. Systematic study of aqueous monoethanolamine (MEA)-based CO_2 capture process: Techno-economic assessment of the MEA process and its improvements. *Applied Energy*, 165, pp.648-659. DOI: 10.1016/j.apenergy.2015.12.109.

Mangalapally, H.P. and Hasse, H., 2011. Pilot plant study of post-combustion carbon dioxide capture by reactive absorption: Methodology, comparison of different structured packings, and comprehensive results for monoethanolamine. *Chemical Engineering Research and Design*, 89(8), pp.1216-1228. DOI: 10.1016/j.cherd.2011.01.013

Michalski, J.A., 2000. Aerodynamic characteristics of flue gas desulfurization spray towers polydispersity consideration. *Industrial & engineering chemistry research*, 39(9), pp.3314-3324. DOI: 10.1021/ie990791h.

Modest, M.F. and Mazumder, S., 2021. Radiative heat transfer. Academic press.

Mojtabi, M., Chadwick, N., Wigley, G. and Helie, J., 2008, September. The effect of flash boiling on break up and atomization in GDI sprays. *In Proceedings of the 22nd European Conference on Liquid Atomization and Spray Systems. ILASS Europe. Como Lake, Italy* (pp. 8-10).

Oshina, I. and Spigulis, J., 2021. Beer–Lambert law for optical tissue diagnostics: current state of the art and the main limitations. *Journal of biomedical optics*, 26(10), pp.100901-100901. DOI: 10/gn63sn

Ouboukhlik, M., Godard, G., Saengkaew, S., Fournier-Salaün, M.C., Estel, L. and Grehan, G., 2015a. Mass transfer evolution in a reactive spray during carbon dioxide capture. Chemical Engineering & Technology, 38(7), pp.1154-1164. DOI: 10.1002/ceat.201400651.

Ouboukhlik, M., Saengkaew, S., Fournier-Salaün, M.C., Estel, L. and Grehan, G., 2015b. Local measurement of mass transfer in a reactive spray for CO2 capture. The Canadian Journal of Chemical Engineering, 93(2), pp.419-426. DOI: 10.1002/cjce.22123.

Pickett, L.M., Genzale, C.L., Bruneaux, G., Malbec, L.M., Hermant, L., Christiansen, C. and Schramm, J., 2010. Comparison of diesel spray combustion in different high-temperature, high-pressure facilities. SAE International Journal

of Engines, 3(2), pp.156-181. DOI: 10.4271/2010-01-2106

Puxty, G., Rowland, R., Allport, A., Yang, Q., Bown, M., Burns, R., Maeder, M. and Attalla, M., 2009. Carbon dioxide postcombustion capture: a novel screening study of the carbon dioxide absorption performance of 76 amines. *Environmental science & technology*, 43(16), pp.6427-6433. DOI: 10.1021/es901376a.

Reitz, R.D., 1990. A photographic study of flash-boiling atomization. *Aerosol Science and Technology*, 12(3), pp.561-569. DOI: 10.1080/02786829008959370.

Ritchie, H., Roser, M., Rosado, P., CO_2 and Greenhouse Gas Emissions (2020), Our world in data, accessed May 19th, 2023, from: www.ourworldindata.org

Rochelle, G.T., 2009. Amine scrubbing for CO_2 capture. *Science*, 325(5948), pp.1652-1654. DOI: 10.1126/science.1176731

Sema, T., Naami, A., Usubharatana, P., Wang, X., Gao, R., Liang, Z., Idem, R. and Tontiwachwuthikul, P., 2013. Mass transfer of CO_2 absorption in hybrid MEA-methanol solvents in packed column. *Energy Procedia*, 37, pp.883-889. DOI: 10.1016/j.egypro.2013.05.181.

Senda, J., Wada, Y., Kawano, D. and Fujimoto, H., 2008. Improvement of combustion and emissions in diesel engines by means of enhanced mixture formation based on flash boiling of mixed fuel. *International Journal of Engine Research*, 9(1), pp.15-27. DOI: 10.1243/14680874JER02007.

Seyboth, O., Zimmermann, S., Heidel, B. and Scheffknecht, G., 2014. Development of a spray scrubbing process for post combustion CO_2 capture with amine based solvents. *Energy Procedia*, 63, pp.1667-1677. DOI: 10/j98k

She, J., 2010. Experimental study on improvement of diesel combustion and emissions using flash boiling injection (No. 2010-01-0341). *SAE Technical Paper*. DOI: 10.4271/2010-01-0341.

Shen, Y., Jiang, C., Zhang, S., Chen, J., Wang, L. and Chen, J., 2018. Biphasic solvent for CO_2 capture: Amine property-performance and heat duty relationship. *Applied energy*, 230, pp.726-733.DOI: 10.1016/j.apenergy.2018.09.005.

Shen, S., Jia, M., Wang, T., Lü, Q. and Sun, K., 2016. Measurement of the droplets sizes of a flash boiling spray using an improved extended glare point velocimetry and sizing. *Experiments in Fluids*, 57, pp.1-16. DOI: 10.1007/s00348-016-2147-3.

Span, R. and Wagner, W., 1996. A new equation of state for carbon dioxide covering the fluid region from the triple-point temperature to 1100 K at pressures up to 800 MPa. *Journal of physical and chemical reference data*, 25(6), pp.1509-1596. DOI: 10.1063/1.555991

Stolaroff, J.K., Keith, D.W. and Lowry, G.V., 2008. Carbon dioxide capture from atmospheric air using sodium hydroxide spray. *Environmental science & technology*, 42(8), pp.2728-2735. DOI: 10/d536hr

Tamhankar, Y., King, B., Whiteley, R., Resetarits, M., Cai, T. and Aichele, C., 2014. Aqueous amine spray absorption and droplet distribution data for CO_2 capture applications. *Energy Procedia*, 63, pp.293-300. DOI: 10.1016/j.egypro.2014.11.032.

UK Department for Energy Security and Net Zero, Department for Business, Energy & Industrial Strategy, and The Rt Hon Boris Johnson MP, The Ten Point Plan for a Green Industrial Revolution (2020), accessed May 19th , 2023, from: www.gov.uk

United Kingdom Accreditation Service, 1997. The expression of uncertainty and confidence in measurement. United Kingdom Accreditation Service.

United Nations Framework Convention on Climate Change, The Paris Agreement, in Report of the conference of the

779 parties to the United Nations framework convention on climate change (21st session, 2015: Paris) (Vol. 4), accessed
780 18th May 2023, from: www.heinonline.org
781 Usubharatana, P. and Tontiwachwuthikul, P., 2009. Enhancement factor and kinetics of CO_2 capture by MEA-methanol
782 hybrid solvents. *Energy Procedia*, 1(1), pp.95-102. DOI: 10.1016/j.egypro.2009.01.015.
783 Vega, F., Sanna, A., Navarrete, B., Maroto-Valer, M.M. and Cortés, V.J., 2014. Degradation of amine-based solvents in
784 CO_2 capture process by chemical absorption. *Greenhouse Gases: Science and Technology*, 4(6), pp.707-733. DOI:
785 10.1002/ghg.1446.
786 Versteeg, G.F., Van Dijck, L.A.J. and van Swaaij, W.P.M., 1996. On the kinetics between CO_2 and alkanolamines both
787 in aqueous and non-aqueous solutions. An overview. *Chemical Engineering Communications*, 144(1), pp.113-158.
788 DOI: 10.1080/00986449608936450.
789 Witlox, H., Harper, M., Bowen, P. and Cleary, V., 2007. Flashing liquid jets and two-phase droplet dispersion: II.
790 Comparison and validation of droplet size and rainout formulations. *Journal of hazardous materials*, 142(3), pp.797-
791 809. DOI: 10.1016/j.jhazmat.2006.06.126.
792 Wu, S., Pan, H., Xu, M., Hung, D.L. and Li, T., 2016. Investigation of rapid atomization and collapse of superheated liq-
793 uid fuel spray under superheated conditions. Atomization and Sprays, 26(12). DOI: 10.1615/AtomizSpr.2016014231.
794 Wu, X., Yu, Y., Qin, Z. and Zhang, Z., 2014. The advances of post-combustion CO_2 capture with chemical solvents:
795 review and guidelines. *Energy Procedia*, 63, pp.1339-1346. DOI: 10.1016/j.egypro.2014.11.143.
796 Xiao, M., Liu, H., Idem, R., Tontiwachwuthikul, P. and Liang, Z., 2016. A study of structure–activity relation-
797 ships of commercial tertiary amines for post-combustion CO2 capture. *Applied energy*, 184, pp.219-229. DOI:
798 10.1016/j.apenergy.2016.10.006.
799 Xu, Y., Chen, X., Zhao, Y. and Jin, B., 2021. Modeling and analysis of CO_2 capture by aqueous ammonia+
800 piperazine blended solution in a spray column. *Separation and Purification Technology*, 267, p.118655. DOI:
801 10.1016/j.seppur.2021.118655.
802 Yang, S., Wang, T., Jia, M., Shen, S. and Yao, Z., 2016. An experimental study on microscopic characteristics of flash
803 boiling spray with extended glare point velocimetry and sizing. *Atomization and Sprays, 26(5)*. DOI: 10.1615/Atom-
804 izSpr.2016014231.
805 Zeng, W., Xu, M., Zhang, G., Zhang, Y. and Cleary, D.J., 2012. Atomization and vaporization for flash-boiling multi-hole
806 sprays with alcohol fuels. *Fuel*, 95, pp.287-297. DOI: 10/dtp2fj
807 Zimmermann, S., Schmid, M.O., Klein, B. and Scheffknecht, G., 2017. Experimental studies on spray absorp-
808 tion with the post combustion CO_2 capture pilot-plant CASPAR. *Energy Procedia*, 114, pp.1325-1333. DOI:
809 10.1016/j.egypro.2017.03.1252.